Cross Ambiguity Function Shaping of Cognitive MIMO Radar: A Synergistic Approach to Antenna Placement and Waveform Design

Zhuang Xie, Linlong Wu, *Senior Member, IEEE*, Xiaotao Huang, *Senior Member, IEEE*, Chongyi Fan, Jiahua Zhu, *Senior Member, IEEE*, and Wei Liu, *Senior Member, IEEE*

***Abstract*— The ambiguity function (AF) is a crucial tool in characterizing the range-angle response of a multiple-input multiple-output (MIMO) radar system, which is intricately influenced by the transmit waveforms, receiving filters and also antenna configurations. Notably, the role of antenna configurations is less explored compared to the well-studied areas of waveforms and filters. In this article, we incorporate antenna positions as an additional design parameter alongside waveforms and filters to optimize the AF in a specific range-angle bin. We employ the mainlobe-to-integrated-sidelobe-level-ratio (MISLR) as a quantitative metric to assess the performance. The resulting optimization problem is inherently nonconvex, encompassing binary and unimodular constraints. To address this challenge, we reformulate the problem, enabling an alternating optimization approach for antenna positions and waveforms. Each iteration involves solving a sequence of quadratic constrained quadratic programming problems for the binarily constrained antenna position optimization and updating the waveforms iteratively via an analytical expression. Our simulation results validate the effectiveness of the proposed method as it achieves higher MISLR with the same number of antennas compared to conventional approaches. Moreover, the optimized antenna configurations notably enhance the balance between angular ambiguity and resolution.**

***Index Terms*— Ambiguity function (AF), antenna positions, majorization–minimization (MM), multiple-input multiple-output (MIMO) radar, waveform design.**

Manuscript received 22 January 2024; revised 30 April 2024; accepted 11 June 2024. Date of publication 17 June 2024; date of current version 27 June 2024. The work of Zhuang Xie, Xiaotao Huang, Chongyi Fan, and Jiahua Zhu was supported by the National Natural Science Foundation of China under Grant 62101573. The work of Linlong Wu was supported by the Luxembourg FNR CORE Project under Grant C22/IS/17391632/METSA and Grant C20/IS/14799710/SENCOM. The work of Wei Liu was supported by the U.K. Engineering and Physical Sciences Research Council under Grant EP/V009419/2. *(Corresponding authors: Linlong Wu; Xiaotao Huang.)*

Zhuang Xie, Xiaotao Huang, and Chongyi Fan are with the College of Electronic Science and Technology, National University of Defense Technology, Changsha 410000, China (e-mail: xiezhuang18@nudt.edu.cn; xthuang@nudt.edu.cn; chongyifan@nudt.edu.cn).

Linlong Wu is with the Interdisciplinary Center for Security, Reliability and Trust (SnT), University of Luxembourg, 4365 Esch-sur-Alzette, Luxembourg (e-mail: linlong.wu@uni.lu).

Jiahua Zhu is with the College of Meteorology and Oceanography, National University of Defense Technology, Changsha 410073, China (e-mail: zhujiahua1019@hotmail.com).

Wei Liu is with the School of Electronic Engineering and Computer Science, Queen Mary University of London, E1 4NS London, U.K. (e-mail: w.liu@qmul.ac.uk).

Digital Object Identifier 10.1109/TGRS.2024.3415428

I. Introduction

THE technology of waveform design in radar systems has indeed seen significant advancements over the past decades, largely attributed to developments in hardware and algorithms [1], [2], [3], [4]. As proven in numerous research works, emitting tailored radar waveforms enables significant improvement in resolution, detection, and estimation performance in the fields of atmospheric remote sensing, meteorological monitoring, and military aviation surveillance [5], [6], [7], [8], [9], [10], [11]. From the perspective of ambiguity function (AF), the problems of waveform design boils down to the one shaping the AF among the range, angle, and frequency dimensions [12], [13], [14], [15], [16], [17].

A. Range-Angle Cross AF

In multiple-input multiple-output (MIMO) radar signal processing, the range-angle response of a mismatched filter to any given range bin l and space direction θ, can be defined as the MIMO range-angle cross AF (RACAF) [12], [18], [19] mathematically given by

$$\chi(l,\theta)=\left|\mathrm{Tr}\left(\mathbf{W}^H\mathbf{J}_l\mathbf{S}\mathbf{a}_{\mathrm{t}}(\theta)\mathbf{a}_{\mathrm{r}}^T(\theta)\right)\right|^2 \tag{1}$$

where $\mathbf{S}=[\mathbf{s}_1,\mathbf{s}_2,\ldots,\mathbf{s}_{N_{\mathrm{t}}}]\in\mathbb{C}^{L\times N_{\mathrm{t}}}$ and $\mathbf{W}=[\mathbf{w}_1,\mathbf{w}_2,\ldots,\mathbf{w}_{N_{\mathrm{r}}}]\in\mathbb{C}^{L\times N_{\mathrm{r}}}$ are the waveform and filter matrix, respectively, with $\mathbf{s}_n$ being the waveform emitted by the nth transmit channel and $\mathbf{w}_n$ being the filter applied at the nth receive channel, L is the length of phase-coded signal, and N_{t} and N_{r} denote, respectively, the number of transmit and receive antennas. The vectors $\mathbf{a}_{\mathrm{t}}(\theta)$ and $\mathbf{a}_{\mathrm{r}}(\theta)$ are, respectively, the transmit and receive steering vectors. The matrix $\mathbf{J}_l\in\mathbb{C}^{L\times L}$ is the shift matrix with its elements given by

$$\mathbf{J}_l(i,j)=\begin{cases}1, & i-j-l=0\\ 0, & i-j-l\neq 0.\end{cases} \tag{2}$$

The RACAF provides a unified perspective on the investigation of clutter suppression or the design of transmit waveforms for MIMO radar. The expression given by (1) is general and encompasses many models in literature as special cases. For example, when the radar transmits identical waveforms among different channels and applies corresponding matched filters at the receiving end, the MIMO radar degenerates into a

© 2024 The Authors. This work is licensed under a Creative Commons Attribution 4.0 License.
For more information, see https://creativecommons.org/licenses/by/4.0/

traditional phased array radar. In this case, the response at range bin l and direction θ can be calculated as

$$\chi_{\mathrm{PA}}(l,\theta)=\left(\left|\mathbf{w}_{\mathrm{t}}^{T}\mathbf{a}_{\mathrm{t}}(\theta)\right|^{2}\left|\mathbf{w}_{\mathrm{r}}^{T}\mathbf{a}_{\mathrm{r}}^{*}(\theta)\right|^{2}\right)\left|\mathbf{s}_{\mathrm{PA}}^{H}\mathbf{J}_{l}\mathbf{s}_{\mathrm{PA}}\right|^{2} \tag{3}$$

where $\mathbf{s}_{\mathrm{PA}}$ stands for the transmitted waveform, and $\mathbf{w}_{\mathrm{t}}$ and $\mathbf{w}_{\mathrm{r}}$ represent the corresponding weighting vectors at transmit and receive end, respectively. For this radar system, the range response and the angular response are separated. More importantly, the range response along different directions are similar, which implies that clutter can only be effectively suppressed in the angle domain via joint transmit and receive beamforming [20], [21], [22]. Furthermore, when $N_{\mathrm{t}}=N_{\mathrm{r}}=1$, (3) reduces to the standard autocorrelation function as

$$\tilde{\chi}_{\mathrm{PA}}(l)=\left|\mathbf{s}_{\mathrm{PA}}^{H}\mathbf{J}_{l}\mathbf{s}_{\mathrm{PA}}\right|^{2} \tag{4}$$

for which the minimization of peak sidelobe level (PSL) or integrated sidelobe level (ISL) has been widely studied in the literature [15], [17], [23], [24], [25], [26].

Back to the RACAF in (1), by defining $\mathbf{s}_{\theta}=\mathbf{S}\mathbf{a}_{\mathrm{t}}(\theta)$ and $\mathbf{w}_{\theta}=\mathbf{W}\mathbf{a}_{\mathrm{r}}^{*}(\theta)$ with θ assumed to be known, we have the equivalent expression

$$\chi_{\theta}(l)=\left|\mathbf{w}_{\theta}^{H}\mathbf{J}_{l}\mathbf{s}_{\theta}\right|^{2} \tag{5}$$

which is exactly the response of mismatched filter $\mathbf{w}_{\theta}$ applied to sequence $\mathbf{s}_{\theta}$ at range bin l as studied in [14], [27], [28], and [29]. Contrary to (3), the range response of the MIMO radar adapts when the angle changes as $\chi_{\theta}(l)$ is parameterized by θ. This feature ensures the applicability of MIMO radar in high-reverberation scenarios where clutter distributions along the range dimension vary dramatically across different angular directions.

B. Motivations and Related Works

Upon a closer examination of the RACAF, as detailed in (5), it becomes evident that the angular variability in the synthesized waveform and filter is a direct consequence of their multiplication with the corresponding transmit vector $\mathbf{a}_{\mathrm{t}}(\theta)$ and receive steering vector $\mathbf{a}_{\mathrm{r}}(\theta)$. This variation is significantly influenced by the array configuration, including factors such as the number, position, and spacing of the antennas [30], [31], [32]. Consequently, it is crucial to include the array configuration in the design process, in addition to the transmit waveform and receive filter. Such integration ensures achieving a desired angular-adaptive range response, which can be flexibly tailored to accommodate varying angular clutter distributions.

When the number of antennas is fixed, array configuration specifically refers to the placement of these antennas [33], [34]. It has been investigated for many applications in radar and communications, such as direction of arrival estimation [35], [36], [37] and spatial beamforming [38], [39], [40], [41], [42], [43], [44]. However, in MIMO radar waveform design, the majority of related researches still focus on optimizing the waveforms on uniform array structure. In these studies, efforts have been made for shaping MIMO beampattern [45], [46], enhancing MIMO detection [18], [19], [47], [48], [49] and estimation [50], [51], [52] performance. As pioneer works, the joint design of MIMO waveform and antenna positions for beampattern matching is investigated in [53], [54], [55], and [56]. In further detail, the mean-square error (MSE) between the template beampattern and the tailored one is minimized in [53] resorting to the alternating direction method of multipliers framework. To circumvent potential performance loss brought by the indirect design through MSE minimization, a direct objective is formulated in [54] which aims to eliminate mainlobe ripple and suppress sidelobe level. Concerning the implementation efficiency and accuracy, a local optimization framework is developed in [55] and an iterative greedy local search approach is proposed in [56]. Although desirable spatial beampatterns can be formed by the above methods, target indication capabilities along range domain are barely guaranteed and the clutters are usually space-time distributed [57], [58]. Furthermore, concerning a complete processing procedure, it is beneficial to take into consideration the receiver end during the joint design.

The above analysis calls for joint consideration of antenna placement and radar waveform and filter to shape the MIMO radar cross AF, which, to the best of our knowledge, has not been addressed before. By leveraging this new degree of freedom (DoF) in antenna placement, the MIMO system is expected to achieve greater flexibility and potentially exceed the performance benchmarks established in previously cited works. Conceptually, incorporating antenna placement into the design of waveforms and filters broadens the ambit of MIMO radar technology. It shifts the notion of independence from being limited to radio frequency (RF) chains to encompassing the antennas themselves. This paradigm illustrates more independence, with each antenna emitting signals independently, in terms of both signal characteristics and spatial positioning.

C. Our Contributions

In light of the discussions presented earlier, this article introduces a novel approach by utilizing antenna placement as an additional DoF. Our objective is to optimize the range-angle response of MIMO radar systems through a comprehensive design strategy that integrates transmit waveforms, receive filters, and antenna positions. This approach is aimed at augmenting the capability of the system in the range-angle domain. Specifically, this joint design strategy can shape a desired pattern of the RACAF to better adapt to the complicated clutter distributions. The contributions of this article are summarized in the following three aspects.

1) Antenna position is introduced for the first time as an extra DoF for local MIMO RACAF shaping besides waveform and filter to achieve superior target indication ability, where MIMO antennas at both the transmit and receive ends are assumed movable among several divided grid points. The concerned RACAF behavior within the interested region is represented by the defined mainlobe-to-integrated-sidelobe-level-ratio (MISLR), which describes the sidelobe level with guaranteed target response. RACAF shaping is formulated as an MISLR maximization problem via the joint design of waveform, filter, and antenna positions.
2) An effective algorithm is developed to deal with the formulated nonconvex joint design problem where complex

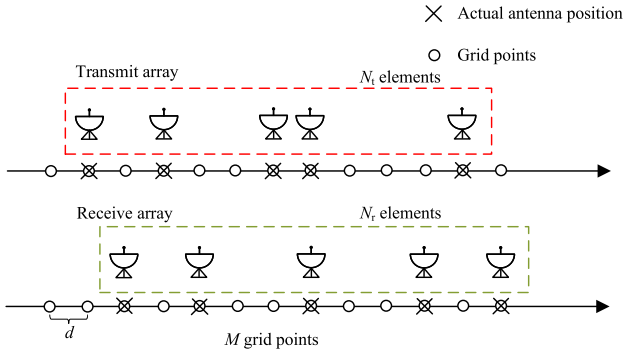

Fig. 1. Representation of the MIMO antenna placement scene where M grid points are considered.

objective function and highly nonconvex restrictions, especially the binary constraints on antenna positions, are involved. Leveraging on an appropriate reformulation of the original problem, we propose to alternately optimize antenna positions and radar waveform. In each cycle, it is proved that the antenna placement subproblem can be tackled by solving a series of quadratic constrained quadratic programming (QCQP) problems. Resorting to the majorization–minimization (MM) framework, the waveform is updated based on an analytical expression. It is analyzed that the generality of the established model and the associated algorithm enables direct applications for other operating scenarios.

3) Simulations are provided to verify the superiority of our proposed scheme. It is shown that integrating antenna position into the design stage brings significant performance enhancement to MIMO radar compared with traditional design schemes where only waveform and filter are adjusted. Furthermore, the results demonstrate that the array configuration optimized by the developed algorithm provides a more desirable RACAF with higher MISLR in comparison with other benchmarks of placement.

The rest of this article is organized as follows: Section II establishes and analyzes the signal model for MIMO radar where the impact of array structure is considered. Section III formulates the joint design problem for RACAF sharping and develops an effective optimization paradigm to enhance MISLR. Simulation results are given in Section IV and conclusions are drawn in Section V.

Notations: $(\cdot)^T$, $(\cdot)^*$, and $(\cdot)^H$ denote transpose, conjugate, and conjugate transpose, respectively. $\mathbb{C}^N$ is the set of N-dimensional complex space. $\Re\{\cdot\}$ and $\arg(\cdot)$ obtains the real part and the phase of a complex argument, respectively. $\mathrm{Tr}(\cdot)$ represents the trace of a square matrix and $\otimes$ denotes the Kronecker product. For a Hermitian matrix $\mathbf{A}$, $\mathbf{A} \succeq 0$ means $\mathbf{A}$ is positive semidefinite. $\mathbf{I}$ denotes the identity matrix.

II. Signal Model and Analysis

As shown in Fig. 1, both the transmit and receiving antennas of an MIMO radar can be freely placed among $M \geq \max\{N_t, N_r\}$ grid points, respectively, with an equal spacing interval d between adjacent grid points. The waveform transmitted via the nth grid point is denoted by $\mathbf{s}_n$ and the filter applied to the mth receiving grid point is denoted by $\mathbf{w}_m$.

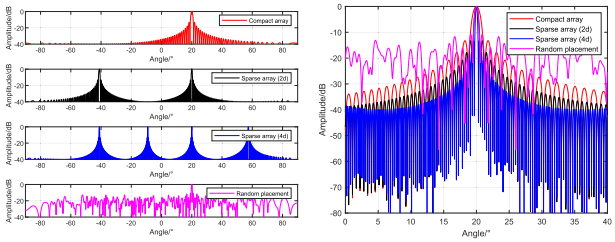

(a) (b)

Fig. 2. Beampattern comparison. (a) Angular ambiguity. (b) Beam resolution.

We define the selection vectors of the transmit and receiving grid points by $\mathbf{p}_t \in \mathbb{C}^M$ and $\mathbf{p}_r \in \mathbb{C}^M$, respectively, and the value of their elements is either 0 or 1. With this definition, the transmit steering vector and receive steering vector of the MIMO radar can be expressed as $\mathbf{a}_t(\theta) = \mathbf{p}_t \odot \mathbf{a}(\theta)$ and $\mathbf{a}_r(\theta) = \mathbf{p}_r \odot \mathbf{a}(\theta)$, where $\mathbf{a}(\theta) \in \mathbb{C}^M$ is the generalized steering vector (without loss of generality, $\mathbf{a}(\theta)$ is utilized for both transmit and receive arrays). Therefore, the RACAF given by (1) can be recast equivalently into

$$\chi(l,\theta) = \left|\mathbf{w}^H(\mathbf{H}(\theta,\mathbf{p}_t,\mathbf{p}_r)\otimes\mathbf{J}_l)\mathbf{s}\right|^2 \tag{6}$$

where $\mathbf{s} = \mathrm{vec}(\mathbf{S}) \in \mathbb{C}^{ML}$, $\mathbf{w} = \mathrm{vec}(\mathbf{W}) \in \mathbb{C}^{ML}$, and $\mathbf{H}(\theta,\mathbf{p}_t,\mathbf{p}_r) = \mathbf{A}(\theta)\mathbf{p}_r\mathbf{p}_t^T\mathbf{A}^T(\theta)$ with $\mathbf{A}(\theta) = \mathrm{diag}\{\mathbf{a}(\theta)\}$.

Recall that the half-wavelength spacing is usually set in a conventional array configuration, beyond which the angular ambiguity will appear. However, increasing the spacing interval will elongate the array aperture,[1] which further leads to a sharper mainlobe or equivalently high angular resolution. In Fig. 2, the beampatterns of an array of the same number of antennas for different spacing intervals are shown. We can see clearly the tradeoff between angular ambiguity and resolution. Although a random placement avoids the periodicity of the steering vector, the resultant sidelobe is at a high level. In this context, by considering the antenna placement or the grid point selection explicitly in the problem formulation, the spacing intervals among antennas will be optimized. Together with the waveform and filter design, it is anticipated that the range-angle response will be well-shaped. In particular, a trade-off between angular ambiguity and resolution will be reached optimally.

The range-angle region of interest is denoted by Ω associated with angular sector Θ and range bins $[-L+1, L-1]$. To measure the response of this region, we resort to the concept of the weighted integrated sidelobe level (WISL) [16], [23], [59], [60]. Note that the original WISL was applied to the range domain, and we extend it to the joint range-angle domain. The WISL in our case is defined as

$$\begin{aligned}\widetilde{\mathrm{WISL}}&(\mathbf{w},\mathbf{s},\mathbf{p}_t,\mathbf{p}_r)\\ &= \sum_{l=-L+1}^{L-1}\int_\Theta \eta(l,\theta)\cdot\chi(l,\theta)\,d\theta\\ &= \sum_{l=-L+1}^{L-1}\int_\Theta \eta(l,\theta)\left|\mathbf{w}^H(\mathbf{H}(\theta,\mathbf{p}_t,\mathbf{p}_r)\otimes\mathbf{J}_l)\mathbf{s}\right|^2 d\theta\end{aligned} \tag{7}$$

[1] A straightforward alternative is increasing the number of antennas still with the half-wavelength spacing interval, which however achieves the benefits at the cost of hardware and power consumption. In this article, this approach serves as the benchmark configuration.

where $\eta(l,\theta)$ represents the weighting parameter at direction θ and range bin l. By splitting the angular sector Θ into $\{\theta_k\}_{k=1}^K$, the WISL can be changed to

$$\begin{aligned}&\mathrm{WISL}(\mathbf{w},\mathbf{s},\mathbf{p}_\mathrm{t},\mathbf{p}_\mathrm{r})\\&\quad=\sum_{l=-L+1}^{L-1}\sum_{k=1}^{K}\eta(l,\theta_k)\cdot\chi(l,\theta_k)\\&\quad=\sum_{l=-L+1}^{L-1}\sum_{k=1}^{K}\eta(l,\theta_k)\left|\mathbf{w}^H(\mathbf{H}(\theta_k,\mathbf{p}_\mathrm{t},\mathbf{p}_\mathrm{r})\otimes\mathbf{J}_l)\mathbf{s}\right|^2.\end{aligned}\tag{8}$$

Consequently, to suppress sidelobes within Ω, we could minimize WISL by optimizing $(\mathbf{w},\mathbf{s},\mathbf{p}_\mathrm{t},\mathbf{p}_\mathrm{r})$.

However, unlike conventional range-Doppler AF shaping [61], the response of RACAF at the target range-angle position is not constant. Without loss of generality, assuming a target located at range 0 and angle θ_{tar}, the corresponding RACAF response at the target location, i.e., mainlobe level (ML), is

$$\begin{aligned}\mathrm{ML}(\mathbf{w},\mathbf{s},\mathbf{p}_\mathrm{t},\mathbf{p}_\mathrm{r})&=\chi(0,\theta_{\mathrm{tar}})\\&=\left|\mathbf{w}^H(\mathbf{H}(\theta_{\mathrm{tar}},\mathbf{p}_\mathrm{t},\mathbf{p}_\mathrm{r})\otimes\mathbf{I})\mathbf{s}\right|^2\end{aligned}\tag{9}$$

which is related to $\mathbf{w}$, $\mathbf{s}$, $\mathbf{p}_\mathrm{t}$, and $\mathbf{p}_\mathrm{r}$, and also changes along θ_{tar}. Based on this observation, merely minimizing the WISL could not guarantee the response at the target range-angle bin, which would eventually lead to a deteriorated target indication performance even though the response at the clutter region is suppressed. Therefore, an appropriate design metric is required to shape the range-angle profile properly taking both target and clutter into consideration.

Inspired by the objective function for the MIMO beampattern sidelobe suppression in [46], we define MISLR as our design metric for sidelobe suppression in the concerned area with a guaranteed target response.[2] The MISLR is defined as

$$\begin{aligned}&\mathrm{MISLR}(\mathbf{w},\mathbf{s},\mathbf{p}_\mathrm{t},\mathbf{p}_\mathrm{r})\\&=\frac{\mathrm{ML}(\mathbf{w},\mathbf{s},\mathbf{p}_\mathrm{t},\mathbf{p}_\mathrm{r})}{\mathrm{WISL}(\mathbf{w},\mathbf{s},\mathbf{p}_\mathrm{t},\mathbf{p}_\mathrm{r})}\\&=\frac{\left|\mathbf{w}^H(\mathbf{H}(\theta_{\mathrm{tar}},\mathbf{p}_\mathrm{t},\mathbf{p}_\mathrm{r})\otimes\mathbf{I})\mathbf{s}\right|^2}{\sum_{l=-L+1}^{L-1}\sum_{k=1}^{K}\eta(l,\theta_k)\left|\mathbf{w}^H(\mathbf{H}(\theta_k,\mathbf{p}_\mathrm{t},\mathbf{p}_\mathrm{r})\otimes\mathbf{J}_l)\mathbf{s}\right|^2}.\end{aligned}\tag{10}$$

Note that the MISLR could be maximized when $\sum_{l=-L+1}^{L-1}\sum_{k=1}^{K}\eta(l,\theta_k)|\mathbf{w}^H(\mathbf{H}(\theta_k,\mathbf{p}_\mathrm{t},\mathbf{p}_\mathrm{r})\otimes\mathbf{J}_l)\mathbf{s}|^2=0$. However, in this case, the value of the numerator is not guaranteed, i.e., the target response can be very small. To ensure proper shaping of the range-angle response for both sidelobes and target areas, we regularize the MISLR with a positive scalar as

$$\begin{aligned}&\widetilde{\mathrm{MISLR}}(\mathbf{w},\mathbf{s},\mathbf{p}_\mathrm{t},\mathbf{p}_\mathrm{r})\\&=\frac{\left|\mathbf{w}^H(\mathbf{H}(\theta_{\mathrm{tar}},\mathbf{p}_\mathrm{t},\mathbf{p}_\mathrm{r})\otimes\mathbf{I})\mathbf{s}\right|^2}{\sum_{l=-L+1}^{L-1}\sum_{k=1}^{K}\eta(l,\theta_k)\left|\mathbf{w}^H(\mathbf{H}(\theta_k,\mathbf{p}_\mathrm{t},\mathbf{p}_\mathrm{r})\otimes\mathbf{J}_l)\mathbf{s}\right|^2+c}\end{aligned}\tag{11}$$

where c is a positive constant scalar.

[2]An alternative objective function can be formulated by integrating the target response into the WISL function as an additional term with a negative weighting coefficient. Although this kind of formulation seems natural, it should be pointed out that the selection of the assigned weighting coefficient is very critical to the result.

III. Problem Formulation and Developed Algorithm

A. Problem Formulation

As per the above illustrations, we aim to jointly design the radar waveform, receive filter as well as antenna positions to shape a desired RACAF shape. Specifically, the response from the sidelobe regions will be suppressed while the target region remains a relatively high response.

Given the number of antennas, the constraints on the selection vectors of the transmit and receiving antenna positions (i.e., $\mathbf{p}_\mathrm{t}$ and $\mathbf{p}_\mathrm{r}$) are

$$\begin{cases}p_{\mathrm{t},m},\,p_{\mathrm{r},m}\in\{0,1\}, & m=1,2,\ldots,M\\ \mathbf{p}_\mathrm{t}^T\mathbf{1}=N_\mathrm{t}, & \mathbf{p}_\mathrm{r}^T\mathbf{1}=N_\mathrm{r}\end{cases}\tag{12}$$

where N_t and N_r are the actual numbers of transmit and receiving antennas, respectively.

Therefore, the problem can be formulated as

$$\tilde{\mathcal{P}}\begin{cases}\max\limits_{\mathbf{w},\mathbf{s},\mathbf{p}_\mathrm{t},\mathbf{p}_\mathrm{r}}\ \widetilde{\mathrm{MISLR}}(\mathbf{w},\mathbf{s},\mathbf{p}_\mathrm{t},\mathbf{p}_\mathrm{r})\\ \text{s.t. }\ p_{\mathrm{r},m},\,p_{\mathrm{t},m}\in\{0,1\}\quad\forall m\\ \quad\mathbf{p}_\mathrm{r}^T\mathbf{1}=N_\mathrm{r},\quad\mathbf{p}_\mathrm{t}^T\mathbf{1}=N_\mathrm{t}\\ \quad|s_l|=1\quad\forall l\\ \quad\|\mathbf{w}\|_2^2=1\end{cases}\tag{13}$$

where the transmit waveforms are restricted to be unimodular without loss of generality.

Remark 1: Beyond existing works focusing solely on the design of radar waveforms and filters, we also exploit antenna positions as an additional DoF to enhance target indication performance, which, to the best of our knowledge, has not been previously considered in the literature. Consequently, the problem becomes nonconvex and involves multiple variables, including discrete ones such as $\mathbf{p}_\mathrm{t}$ and $\mathbf{p}_\mathrm{r}$, which collectively increase the complexity of solving $\tilde{\mathcal{P}}$.

B. Developed Algorithm

In this section, an alternating optimization framework is devised to monotonically enhancing the MISLR. To begin with, note that based on the transformation $c=((\mathbf{w}^H c\mathbf{I}\mathbf{w})/\|\mathbf{w}\|_2^2)$, we can equivalently address the following problem:

$$\tilde{\mathcal{P}}\begin{cases}\max\limits_{\mathbf{w},\mathbf{s},\mathbf{p}_\mathrm{t},\mathbf{p}_\mathrm{r}}\ \dfrac{\left|\mathbf{w}^H\boldsymbol{\Psi}_{\mathrm{tar}}(\mathbf{p}_\mathrm{t},\mathbf{p}_\mathrm{r})\mathbf{s}\right|^2}{\mathbf{w}^H(\boldsymbol{\Phi}_{\mathrm{sl}}(\mathbf{s},\mathbf{p}_\mathrm{t},\mathbf{p}_\mathrm{r})+c\mathbf{I})\mathbf{w}}\\ \text{s.t. }\ p_{\mathrm{r},m},\,p_{\mathrm{t},m}\in\{0,1\}\quad\forall m\\ \quad\mathbf{p}_\mathrm{r}^T\mathbf{1}=N_\mathrm{r},\quad\mathbf{p}_\mathrm{t}^T\mathbf{1}=N_\mathrm{t}\\ \quad|s_l|=1\quad\forall l\\ \quad\|\mathbf{w}\|_2^2=1\end{cases}\tag{14}$$

where $\boldsymbol{\Psi}_{\mathrm{tar}}(\mathbf{p}_\mathrm{t},\mathbf{p}_\mathrm{r})=\mathbf{H}(\theta_{\mathrm{tar}},\mathbf{p}_\mathrm{t},\mathbf{p}_\mathrm{r})\otimes\mathbf{I}$, $\boldsymbol{\Phi}_{\mathrm{sl}}(\mathbf{s},\mathbf{p}_\mathrm{t},\mathbf{p}_\mathrm{r})=\sum_{l=-L+1}^{L-1}\sum_{k=1}^{K}\eta(l,\theta_k)\boldsymbol{\Psi}_{l,k}\mathbf{s}\mathbf{s}^H\boldsymbol{\Psi}_{l,k}^H$ with $\boldsymbol{\Psi}_{l,k}(\mathbf{p}_\mathrm{t},\mathbf{p}_\mathrm{r})=\mathbf{H}(\theta_k,\mathbf{p}_\mathrm{t},\mathbf{p}_\mathrm{r})\otimes\mathbf{J}_l$. The optimization with respect to the filter is a Rayleigh quotient problem [62] which has closed-form solution $\mathbf{w}=((\boldsymbol{\Phi}_{\mathrm{sl}}(\mathbf{s},\mathbf{p}_\mathrm{t},\mathbf{p}_\mathrm{r})+c\mathbf{I})^{-1}\boldsymbol{\Psi}_{\mathrm{tar}}(\mathbf{p}_\mathrm{t},\mathbf{p}_\mathrm{r})\mathbf{s})/(\|(\boldsymbol{\Phi}_{\mathrm{sl}}(\mathbf{s},\mathbf{p}_\mathrm{t},\mathbf{p}_\mathrm{r})+c\mathbf{I})^{-1}\boldsymbol{\Psi}_{\mathrm{tar}}(\mathbf{p}_\mathrm{t},\mathbf{p}_\mathrm{r})\mathbf{s}\|_2)$.

Therefore, the resultant problem can be reformulated as

$$\mathcal{P}\begin{cases}\max\limits_{\mathbf{s},\mathbf{p}_\mathrm{t},\mathbf{p}_\mathrm{r}} f(\mathbf{s},\mathbf{p}_\mathrm{t},\mathbf{p}_\mathrm{r}) \\ \text{s.t. } p_{\mathrm{r},m},\quad p_{\mathrm{t},m}\in\{0,1\}\ \forall m \\ \quad \mathbf{p}_\mathrm{r}^T\mathbf{1}=N_\mathrm{r},\quad \mathbf{p}_\mathrm{t}^T\mathbf{1}=N_\mathrm{t} \\ \quad |s_l|=1\quad \forall l\end{cases} \tag{15}$$

where $f(\mathbf{s},\mathbf{p}_\mathrm{t},\mathbf{p}_\mathrm{r})$ denote the objective function for simplicity given by $f(\mathbf{s},\mathbf{p}_\mathrm{t},\mathbf{p}_\mathrm{r}) = \mathbf{s}^H\boldsymbol{\Psi}_{\mathrm{tar}}^H(\mathbf{p}_\mathrm{t},\mathbf{p}_\mathrm{r})(\boldsymbol{\Phi}_{\mathrm{sl}}(\mathbf{s},\mathbf{p}_\mathrm{t},\mathbf{p}_\mathrm{r}) + c\mathbf{I})^{-1}\boldsymbol{\Psi}_{\mathrm{tar}}(\mathbf{p}_\mathrm{t},\mathbf{p}_\mathrm{r})\mathbf{s}$.

We subsequently solve $\mathcal{P}$ by alternately addressing the following two subproblems:

$$\mathcal{P}_a\begin{cases}\max\limits_{\mathbf{p}_\mathrm{t},\mathbf{p}_\mathrm{r}} f(\mathbf{s}_{(q-1)},\mathbf{p}_\mathrm{t},\mathbf{p}_\mathrm{r}) \\ \text{s.t. } p_{\mathrm{r},m},\quad p_{\mathrm{t},m}\in\{0,1\}\ \forall m \\ \quad \mathbf{p}_\mathrm{r}^T\mathbf{1}=N_\mathrm{r},\quad \mathbf{p}_\mathrm{t}^T\mathbf{1}=N_\mathrm{t}\end{cases} \tag{16}$$

and

$$\mathcal{P}_b\begin{cases}\max\limits_{\mathbf{s}} f(\mathbf{s},\mathbf{p}_{\mathrm{t},(q)},\mathbf{p}_{\mathrm{r},(q)}) \\ \text{s.t. } |s_l|=1\quad \forall l\end{cases} \tag{17}$$

where $(\mathbf{s}_{(q)},\mathbf{p}_{\mathrm{t},(q)},\mathbf{p}_{\mathrm{r},(q)})$ is the optimized result at the qth iteration.

1) Optimization of MIMO Antenna Positions: When the waveform is fixed as $\mathbf{s}_{(q-1)}$, $\mathcal{P}_a$ can be further divided into two similar subproblems

$$\mathcal{P}_{a,\mathrm{t}}\begin{cases}\max\limits_{\mathbf{p}_\mathrm{t}} f(\mathbf{s}_{(q-1)},\mathbf{p}_\mathrm{t},\mathbf{p}_{\mathrm{r},(q-1)}) \\ \text{s.t. } p_{\mathrm{t},m}\in\{0,1\}\quad \forall m \\ \quad \mathbf{p}_\mathrm{t}^T\mathbf{1}=N_\mathrm{t}\end{cases} \tag{18}$$

and

$$\mathcal{P}_{a,\mathrm{r}}\begin{cases}\max\limits_{\mathbf{p}_\mathrm{r}} f(\mathbf{s}_{(q-1)},\mathbf{p}_{\mathrm{t},(q)},\mathbf{p}_\mathrm{r}) \\ \text{s.t. } p_{\mathrm{r},m}\in\{0,1\}\quad \forall m \\ \quad \mathbf{p}_\mathrm{r}^T\mathbf{1}=N_\mathrm{r}.\end{cases} \tag{19}$$

It can be easily observed that besides the complex objective function, another challenge results from the highly nonconvex discrete constraints $p_{\mathrm{r},m}, p_{\mathrm{t},m}\in\{0,1\}, \forall m$. Herein, we prove the following proposition that $\mathcal{P}_{a,\mathrm{t}}$ and $\mathcal{P}_{a,\mathrm{r}}$ can be addressed by solving a series of convex QCQP problems.

Proposition 1: The solving processes of (18) and (19) are similar. Specifically, their solution can be obtained by solving a series of problems $\{\tilde{\mathcal{P}}_{a,\mathrm{t}}^{(i)}\}_{i=1}^{\infty}$ and $\{\tilde{\mathcal{P}}_{a,\mathrm{r}}^{(h)}\}_{h=1}^{\infty}$ to convergence and the exact formulation of $\tilde{\mathcal{P}}_{a,\mathrm{t}}^{(i)}$ and $\tilde{\mathcal{P}}_{a,\mathrm{r}}^{(h)}$ are given as

$$\tilde{\mathcal{P}}_{a,\mathrm{t}}^{(i)}\begin{cases}\max\limits_{\mathbf{p}_\mathrm{t},\mu_t} 2\Re\left\{\mathbf{v}_\mathrm{t}^{(i-1)H}\boldsymbol{\Upsilon}_{\mathrm{tar}}\mathbf{p}_\mathrm{t}\right\} - \mathbf{p}_\mathrm{t}^T\boldsymbol{\Xi}_\mathrm{t}^{(i-1)}\mathbf{p}_\mathrm{t} - \rho_\mathrm{t}^{(i-1)}\mu_\mathrm{t} \\ \text{s.t. } p_{\mathrm{t},m}\in[0,1]\quad \forall m \\ \quad \mathbf{p}_\mathrm{t}^T\mathbf{1}=N_\mathrm{t} \\ \quad \mathbf{p}_\mathrm{t}^T\mathbf{p}_\mathrm{t}\le N_\mathrm{t} \\ \quad 2\mathbf{p}_\mathrm{t}^T\mathbf{p}_\mathrm{t}^{(i-1)} - \|\mathbf{p}_\mathrm{t}^{(i-1)}\|_2^2 \ge N_\mathrm{t}-\mu_\mathrm{t} \\ \quad \mu_\mathrm{t}\ge 0 \\ \quad 2\Re\left\{\mathbf{v}_\mathrm{t}^{(i-1)H}\boldsymbol{\Upsilon}_{\mathrm{tar}}\mathbf{p}_\mathrm{t}\right\} - \mathbf{p}_\mathrm{t}^T\boldsymbol{\Xi}_\mathrm{t}^{(i-1)}\mathbf{p}_\mathrm{t} \\ \quad \ge \widetilde{\mathrm{MISLR}}(\mathbf{p}_\mathrm{t}^{(i-1)})\end{cases} \tag{20}$$

and

$$\tilde{\mathcal{P}}_{a,\mathrm{r}}^{(h)}\begin{cases}\max\limits_{\mathbf{p}_\mathrm{r},\mu_r} 2\Re\left\{\mathbf{v}_\mathrm{r}^{(h-1)H}\boldsymbol{\Gamma}_{\mathrm{tar}}\mathbf{p}_\mathrm{r}\right\} - \mathbf{p}_\mathrm{r}^T\boldsymbol{\Xi}_\mathrm{r}^{(h-1)}\mathbf{p}_\mathrm{r} - \rho_\mathrm{r}^{(h-1)}\mu_\mathrm{r} \\ \text{s.t. } p_{\mathrm{r},m}\in[0,1]\quad \forall m \\ \quad \mathbf{p}_\mathrm{r}^T\mathbf{1}=N_\mathrm{r} \\ \quad \mathbf{p}_\mathrm{r}^T\mathbf{p}_\mathrm{r}\le N_\mathrm{r} \\ \quad 2\mathbf{p}_\mathrm{r}^T\mathbf{p}_\mathrm{r}^{(h-1)} - \|\mathbf{p}_\mathrm{r}^{(h-1)}\|_2^2 \ge N_\mathrm{r}-\mu_\mathrm{r} \\ \quad \mu_\mathrm{r}\ge 0 \\ \quad 2\Re\left\{\mathbf{v}_\mathrm{r}^{(h-1)H}\boldsymbol{\Gamma}_{\mathrm{tar}}\mathbf{p}_\mathrm{r}\right\} - \mathbf{p}_\mathrm{r}^T\boldsymbol{\Xi}_\mathrm{r}^{(h-1)}\mathbf{p}_\mathrm{r} \\ \quad \ge \widetilde{\mathrm{MISLR}}(\mathbf{p}_\mathrm{r}^{(h-1)})\end{cases} \tag{21}$$

where $\rho_\mathrm{t}^{(i-1)}\mu_\mathrm{t}$ and $\rho_\mathrm{r}^{(h-1)}\mu_\mathrm{r}$ are the penalty terms with $\{\mu_\mathrm{t},\mu_\mathrm{r}\}$ representing the slack variables, and $\{\rho_\mathrm{t}^{(i-1)},\rho_\mathrm{r}^{(h-1)}\}$ denoting the parameters controlling the slack variables. $\boldsymbol{\Xi}_\mathrm{t}^{(i-1)} = \sum_{l=-L+1}^{L-1}\sum_{k=1}^{K}\eta(l,\theta_k)\boldsymbol{\Upsilon}_{l,k}^H\mathbf{v}_\mathrm{t}^{(i-1)}\mathbf{v}_\mathrm{t}^{(i-1)H}\boldsymbol{\Upsilon}_{l,k}$ and $\boldsymbol{\Xi}_\mathrm{r}^{(h-1)} = \sum_{l=-L+1}^{L-1}\sum_{k=1}^{K}\eta(l,\theta_k)\boldsymbol{\Gamma}_{l,k}^H\mathbf{v}_\mathrm{r}^{(h-1)}\mathbf{v}_\mathrm{r}^{(h-1)H}\boldsymbol{\Gamma}_{l,k}$ with $\mathbf{v}_\mathrm{t}^{(i-1)} = (\boldsymbol{\Phi}_{\mathrm{sl}}(\mathbf{p}_\mathrm{t}^{(i-1)}) + c\mathbf{I})^{-1}\boldsymbol{\Upsilon}_{\mathrm{tar}}\mathbf{p}_\mathrm{t}^{(i-1)}$ and $\mathbf{v}_\mathrm{r}^{(h-1)} = (\boldsymbol{\Phi}_{\mathrm{sl}}(\mathbf{p}_\mathrm{r}^{(h-1)}) + c\mathbf{I})^{-1}\boldsymbol{\Gamma}_{\mathrm{tar}}\mathbf{p}_\mathrm{r}^{(h-1)}$.

Proof: See Appendix. ∎

According to Proposition 1, we can address $\mathcal{P}_{a,\mathrm{t}}$ and $\mathcal{P}_{a,\mathrm{r}}$ by sequentially solving $\{\tilde{\mathcal{P}}_{a,\mathrm{t}}^{(i)}\}_{i=1}^{\infty}$ and $\{\tilde{\mathcal{P}}_{a,\mathrm{r}}^{(h)}\}_{h=1}^{\infty}$, respectively. It is seen that $\tilde{\mathcal{P}}_{a,\mathrm{t}}^{(i)}$ and $\tilde{\mathcal{P}}_{a,\mathrm{r}}^{(h)}$ are convex and can be effectively solved via CVX [63].

It is worth mentioning that a reasonable choice is to further majorize the quadratic objective of $\tilde{\mathcal{P}}_{a,\mathrm{t}}^{(i)}$ into a linear form resorting to the inequality given in [47]. In particular, the following constraint holds:

$$\begin{aligned}\mathbf{p}_\mathrm{t}^T\boldsymbol{\Xi}_\mathrm{t}^{(i-1)}\mathbf{p}_\mathrm{t} \le \lambda\|\mathbf{p}_\mathrm{t}\|_2^2 + 2\Re\left\{\mathbf{p}_\mathrm{t}^T(\boldsymbol{\Xi}_\mathrm{t}^{(i-1)}-\lambda\mathbf{I})\mathbf{p}_\mathrm{t}^{(i-1)}\right\} \\ - \mathbf{p}_\mathrm{t}^{(i-1)T}(\boldsymbol{\Xi}_\mathrm{t}^{(i-1)}-\lambda\mathbf{I})\mathbf{p}_\mathrm{t}^{(i-1)}\end{aligned} \tag{22}$$

where λ can be chosen as the trace of $\boldsymbol{\Xi}_\mathrm{t}^{(i-1)}$. The quadratic term $\lambda\|\mathbf{p}_\mathrm{t}\|_2^2$ becomes constant resorting to the fact that $\mathbf{p}_\mathrm{t}^T\mathbf{p}_\mathrm{t}=N_\mathrm{t}$. Mathematically, a linear majorizer to the quadratic component $-\mathbf{p}_\mathrm{t}^T\boldsymbol{\Xi}_\mathrm{t}^{(i-1)}\mathbf{p}_\mathrm{t}$ can be obtained as $-2\Re\{\mathbf{p}_\mathrm{t}^T(\boldsymbol{\Xi}_\mathrm{t}^{(i-1)}-\lambda\mathbf{I})\mathbf{p}_\mathrm{t}^{(i-1)}\}$. Hence, $\tilde{\mathcal{P}}_{a,\mathrm{t}}^{(i)}$ can further majorized into

$$\tilde{\mathcal{P}}_{a,\mathrm{t}}^{\prime(i)}\begin{cases}\max\limits_{\mathbf{p}_\mathrm{t}} \Re\left\{\mathbf{p}_\mathrm{t}^T\tilde{\mathbf{v}}_\mathrm{t}^{(i-1)}\right\} \\ \text{s.t. } p_{\mathrm{t},m}\in\{0,1\}\quad \forall m \\ \quad \mathbf{p}_\mathrm{t}^T\mathbf{1}=N_\mathrm{t}\end{cases} \tag{23}$$

where $\tilde{\mathbf{v}}_\mathrm{t}^{(i-1)} = \boldsymbol{\Upsilon}_{\mathrm{tar}}^H\mathbf{v}_\mathrm{t}^{(i-1)} - (\boldsymbol{\Xi}_\mathrm{t}^{(i-1)}-\lambda\mathbf{I})\mathbf{p}_\mathrm{t}^{(i-1)}$. The solution of $\tilde{\mathcal{P}}_{a,\mathrm{t}}^{\prime(i)}$ can be directly given by setting the positions of $\mathbf{p}_\mathrm{t}$ corresponding to the N_t largest elements of $\Re\{\tilde{\mathbf{v}}_\mathrm{t}^{(i-1)}\}$ to be one and the rest to be zero. However, further majorization of the objective into a linear form also makes the optimization process looser, and in terms of the practical application and performance in our simulations, it is verified that the discrete feasible constraints of $\mathbf{p}_\mathrm{t}$ make the iteration process fixed at the initial point in most cases.

2) Optimization of MIMO Waveform: Similar to the procedure of antenna position optimization, we also optimize the MIMO radar waveform under the MM framework in this section. Specifically, leveraging on the constrained energy of transmitted waveform, we first majorize the objective function of the waveform optimization subproblem into a

Algorithm 1 Alternating Optimization-Based Framework for Solving $\mathcal{P}$

Input: Number of grid points M, number of MIMO transmit antennas N_{t}, number of MIMO receive antennas N_{r}, weighting coefficients $\eta(l,\theta)$, waveform length L.

1: Set $q=1$, select initial $\mathbf{s}_{(0)}$, $\mathbf{p}_{\mathrm{t},(0)}$ and $\mathbf{p}_{\mathrm{r},(0)}$.
2: Update $\mathbf{p}_{\mathrm{t},(q)}$ by sequentially solving $\{\tilde{\mathcal{P}}_{a,\mathrm{t}}^{(i)}\}_{i=1}^{\infty}$ to convergence.
3: Update $\mathbf{p}_{\mathrm{r},(q)}$ by sequentially solving $\{\tilde{\mathcal{P}}_{a,\mathrm{r}}^{(h)}\}_{h=1}^{\infty}$ to convergence.
4: Update $\mathbf{s}_{(q)}$ by iterating the expression (25) to convergence.
5: **if** Converges **then**
6: Cease the algorithm.
7: **else**
8: $q \leftarrow q+1$ and go to step 2.
9: **end if**

Output: Optimized MIMO transmit array structure $\mathbf{p}_{\mathrm{t},\star}=\mathbf{p}_{\mathrm{t},(q)}$, waveform $\mathbf{s}_{\star}=\mathbf{s}_{(q)}$, receive array structure $\mathbf{p}_{\mathrm{r},\star}=\mathbf{p}_{\mathrm{r},(q)}$ and filter which is calculated as

$$\mathbf{w}_{\star}=\frac{\left(\boldsymbol{\Phi}_{\mathrm{sl}}(\mathbf{s}_{\star},\mathbf{p}_{\mathrm{t},\star},\mathbf{p}_{\mathrm{r},\star})+c\mathbf{I}\right)^{-1}\boldsymbol{\Psi}_{\mathrm{tar}}(\mathbf{p}_{\mathrm{t},\star},\mathbf{p}_{\mathrm{r},\star})\mathbf{s}_{\star}}{\|\left(\boldsymbol{\Phi}_{\mathrm{sl}}(\mathbf{s}_{\star},\mathbf{p}_{\mathrm{t},\star},\mathbf{p}_{\mathrm{r},\star})+c\mathbf{I}\right)^{-1}\boldsymbol{\Psi}_{\mathrm{tar}}(\mathbf{p}_{\mathrm{t},\star},\mathbf{p}_{\mathrm{r},\star})\mathbf{s}_{\star}\|_2}.$$

linear form $\Re\{\mathbf{s}^H(\boldsymbol{\Psi}_{\mathrm{tar}}^H\boldsymbol{\kappa}^{(u-1)}-(\boldsymbol{\Xi}_{\mathrm{s}}^{(u-1)}-\lambda_{\mathrm{s}}^{(u-1)}\mathbf{I})\mathbf{s}^{(u-1)})\}$, where $\boldsymbol{\kappa}^{(u-1)}=(\boldsymbol{\Phi}_{\mathrm{sl}}^{(u-1)}+c\mathbf{I})^{-1}\boldsymbol{\Psi}_{\mathrm{tar}}\mathbf{s}^{(u-1)}$ with $\mathbf{s}^{(u-1)}$ being the optimized result at the $(u-1)$th iteration, $\boldsymbol{\Xi}_{\mathrm{s}}^{(u-1)}=\sum_{l=-L+1}^{L-1}\sum_{k=1}^{K}\eta(l,\theta_k)\boldsymbol{\Psi}_{l,k}^H\boldsymbol{\kappa}^{(u-1)}\boldsymbol{\kappa}^{(u-1)H}\boldsymbol{\Psi}_{l,k}$ and $\lambda_{\mathrm{s}}^{(u-1)}$ is a scalar larger than the maximum eigenvalue of $\boldsymbol{\Xi}_{\mathrm{s}}^{(u-1)}$ and can be chosen as $\mathrm{Tr}(\boldsymbol{\Xi}_{\mathrm{s}}^{(u-1)})$. The resultant maximization problem at the uth iteration based on the MM framework is formulated as

$$\tilde{\mathcal{P}}_b^{(u)}\begin{cases}\max\limits_{\mathbf{s}}\ \Re\left\{\mathbf{s}^H\left(\boldsymbol{\Psi}_{\mathrm{tar}}^H\boldsymbol{\kappa}^{(u-1)}-(\boldsymbol{\Xi}_{\mathrm{s}}^{(u-1)}-\lambda_{\mathrm{s}}^{(u-1)}\mathbf{I})\mathbf{s}^{(u-1)}\right)\right\}\\ \text{s.t. } |s_l|=1\quad \forall l\end{cases}\tag{24}$$

and its closed-form solution can be given directly as

$$\mathbf{s}=e^{j\arg\{\boldsymbol{\Psi}_{\mathrm{tar}}^H\boldsymbol{\kappa}^{(u-1)}-(\boldsymbol{\Xi}_{\mathrm{s}}^{(u-1)}-\lambda_{\mathrm{s}}^{(u-1)}\mathbf{I})\mathbf{s}^{(u-1)}\}}.\tag{25}$$

Therefore, by sequentially updating the MIMO waveform based on (25), the solution to $\mathcal{P}_b$ can be found.

C. Algorithm Summary and Complexity Analysis

The main optimization procedure of the proposed scheme is summarized in Algorithm 1.

The main complexity of the proposed scheme is linear with the number of iterations. With reference to solution of $\tilde{\mathcal{P}}_{a,\mathrm{t}}^{(i)}$ and $\tilde{\mathcal{P}}_{a,\mathrm{r}}^{(h)}$, each optimization can be obtained in polynomial time with a computational cost of $\mathcal{O}(M^3)$. As for the waveform optimization part, the computation cost per iteration within the MM framework comes from the following aspects: the calculation of κ, $\boldsymbol{\Xi}_{\mathrm{s}}^{(u-1)}$ and $\lambda_{\mathrm{s}}^{(u-1)}$. The computation cost of $\lambda_{\mathrm{s}}^{(u-1)}$ is $\mathcal{O}(ML)$ since it is computed as $\mathrm{Tr}(\boldsymbol{\Xi}_{\mathrm{s}}^{(u-1)})$. Due to the involved inversion operation, the cost of calculating κ is $\mathcal{O}(M^3L^3)$.

D. Extension to the Range-Angle-Doppler Domain

Suppose the MIMO radar transmits a burst of Q pulses to illuminate the scene. For the qth pulse, the MIMO waveform matrix is denoted by $\mathbf{S}_q\in\mathbb{C}^{L\times N_{\mathrm{t}}}$ and the corresponding filter matrix at the receiving end is denoted by $\mathbf{W}_q\in\mathbb{C}^{L\times N_{\mathrm{r}}}$. The response of MIMO radar to the range-angle-Doppler cell (l,θ,v) can be calculated as

$$\begin{aligned}\chi_{\mathrm{mp}}(l,\theta,v)&=\left|\mathrm{Tr}\left(\mathbf{W}_{\mathrm{mp}}^H(\mathbf{A}_{\mathrm{st}}(v)\otimes\mathbf{J}_l)\mathbf{S}_{\mathrm{mp}}\mathbf{a}_{\mathrm{t}}(\theta)\mathbf{a}_{\mathrm{r}}^T(\theta)\right)\right|^2\\&=\left|\mathbf{w}_{\mathrm{mp}}^H\boldsymbol{\Psi}_{\mathrm{mp}}(\mathbf{p}_{\mathrm{t}},\mathbf{p}_{\mathrm{r}})\mathbf{s}_{\mathrm{mp}}\right|^2\\&=\left|\mathbf{w}_{\mathrm{mp}}^H\boldsymbol{\Gamma}_{\mathrm{mp}}(\mathbf{p}_{\mathrm{t}},\mathbf{s}_{\mathrm{mp}})\mathbf{p}_{\mathrm{r}}\right|^2\\&=\left|\mathbf{w}_{\mathrm{mp}}^H\boldsymbol{\Upsilon}_{\mathrm{mp}}(\mathbf{s}_{\mathrm{mp}},\mathbf{p}_{\mathrm{r}})\mathbf{p}_{\mathrm{t}}\right|^2\end{aligned}\tag{26}$$

where $\mathbf{S}_{\mathrm{mp}}=[\mathbf{S}_1^T,\mathbf{S}_2^T,\ldots,\mathbf{S}_Q^T]^T\in\mathbb{C}^{QL\times N_{\mathrm{t}}}$, $\mathbf{W}_{\mathrm{mp}}=[\mathbf{W}_1^T,\mathbf{W}_2^T,\ldots,\mathbf{W}_Q^T]^T\in\mathbb{C}^{QL\times N_{\mathrm{r}}}$, $\mathbf{A}_{\mathrm{st}}(v)=\mathrm{diag}\{\mathbf{a}_{\mathrm{st}}(v)\}$ with $\mathbf{a}_{\mathrm{st}}(v)\in\mathbb{C}^Q$ being the slow-time steering vector, $\mathbf{w}_{\mathrm{mp}}=\mathrm{vec}(\mathbf{W}_{\mathrm{mp}})$, and $\mathbf{s}_{\mathrm{mp}}=\mathrm{vec}(\mathbf{S}_{\mathrm{mp}})$, $\boldsymbol{\Psi}_{\mathrm{mp}}(\mathbf{p}_{\mathrm{t}},\mathbf{p}_{\mathrm{r}})=\mathbf{H}(\theta,\mathbf{p}_{\mathrm{t}},\mathbf{p}_{\mathrm{r}})\otimes\mathbf{A}_{\mathrm{st}}(v)\otimes\mathbf{J}_l$, $\boldsymbol{\Gamma}_{\mathrm{mp}}(\mathbf{p}_{\mathrm{t}},\mathbf{s}_{\mathrm{mp}})=\mathbf{A}(\theta)\otimes((\mathbf{A}_{\mathrm{st}}(v)\otimes\mathbf{J}_l)\mathbf{S}_{\mathrm{mp}}\mathbf{A}(\theta)\mathbf{p}_{\mathrm{t}})$ and $\boldsymbol{\Upsilon}_{\mathrm{mp}}(\mathbf{s}_{\mathrm{mp}},\mathbf{p}_{\mathrm{r}})=(\mathbf{A}(\theta)\mathbf{p}_{\mathrm{r}})\otimes((\mathbf{A}_{\mathrm{st}}(v)\otimes\mathbf{J}_l)\mathbf{S}_{\mathrm{mp}}\mathbf{A}(\theta))$. When $Q=1$, namely the single pulse case, (26) reduces to the situation we address in this article. Furthermore, if we are concerned about the disturbance suppression within angle and Doppler domain from a specific range-angle cell under test, we modulate the transmit waveform among pulses and channels based on an identical fast time waveform. Denote by $\tilde{\mathbf{S}}_{\mathrm{mp}}=[\tilde{\mathbf{s}}_1,\tilde{\mathbf{s}}_2,\ldots,\tilde{\mathbf{s}}_{N_{\mathrm{t}}}]\in\mathbb{C}^{Q\times N_{\mathrm{t}}}$, the MIMO coding matrix with $\tilde{\mathbf{s}}_n\in\mathbb{C}^Q$ representing the slow-time coding vector of the nth channel, and $\tilde{\mathbf{W}}_{\mathrm{mp}}=[\tilde{\mathbf{w}}_1,\tilde{\mathbf{w}}_2,\ldots,\tilde{\mathbf{w}}_{N_{\mathrm{r}}}]\in\mathbb{C}^{Q\times N_{\mathrm{r}}}$ stands for the filter matrix applied at the receive end with $\tilde{\mathbf{w}}_n\in\mathbb{C}^Q$ being the slow-time filter applied to the nth receive channel. Under this consideration, the response of MIMO radar at the angle-Doppler cell (θ,v) can be expressed as

$$\begin{aligned}\chi(\theta,v)&=\left|\mathrm{Tr}\left(\tilde{\mathbf{W}}_{\mathrm{mp}}^H\mathbf{A}_{\mathrm{st}}(v)\tilde{\mathbf{S}}_{\mathrm{mp}}\mathbf{a}_{\mathrm{t}}(\theta)\mathbf{a}_{\mathrm{r}}^T(\theta)\right)\right|^2\\&=\left|\tilde{\mathbf{w}}_{\mathrm{mp}}^H\tilde{\boldsymbol{\Psi}}_{\mathrm{mp}}(\mathbf{p}_{\mathrm{t}},\mathbf{p}_{\mathrm{r}})\tilde{\mathbf{s}}_{\mathrm{mp}}\right|^2\\&=\left|\tilde{\mathbf{w}}_{\mathrm{mp}}^H\tilde{\boldsymbol{\Gamma}}_{\mathrm{mp}}(\mathbf{p}_{\mathrm{t}},\tilde{\mathbf{s}}_{\mathrm{mp}})\mathbf{p}_{\mathrm{r}}\right|^2\\&=\left|\tilde{\mathbf{w}}_{\mathrm{mp}}^H\tilde{\boldsymbol{\Upsilon}}_{\mathrm{mp}}(\tilde{\mathbf{s}}_{\mathrm{mp}},\mathbf{p}_{\mathrm{r}})\mathbf{p}_{\mathrm{t}}\right|^2\end{aligned}\tag{27}$$

where $\tilde{\boldsymbol{\Psi}}_{\mathrm{mp}}(\mathbf{p}_{\mathrm{t}},\mathbf{p}_{\mathrm{r}})=\mathbf{H}(\theta,\mathbf{p}_{\mathrm{t}},\mathbf{p}_{\mathrm{r}})\otimes\mathbf{A}_{\mathrm{st}}(v)$, $\tilde{\boldsymbol{\Gamma}}_{\mathrm{mp}}(\mathbf{p}_{\mathrm{t}},\tilde{\mathbf{s}}_{\mathrm{mp}})=\mathbf{A}(\theta)\otimes(\mathbf{A}_{\mathrm{st}}(v)\tilde{\mathbf{S}}_{\mathrm{mp}}\mathbf{A}(\theta)\mathbf{p}_{\mathrm{t}})$, and $\tilde{\boldsymbol{\Upsilon}}_{\mathrm{mp}}(\tilde{\mathbf{s}}_{\mathrm{mp}},\mathbf{p}_{\mathrm{r}})=(\mathbf{A}(\theta)\mathbf{p}_{\mathrm{r}})\otimes(\mathbf{A}_{\mathrm{st}}(v)\tilde{\mathbf{S}}_{\mathrm{mp}}\mathbf{A}(\theta))$.

It can be seen that the above expressions for MIMO response can both be regarded as direct transformation of the established model for MIMO antenna position optimization by replacing $\mathbf{J}_l$ with $\mathbf{A}_{\mathrm{st}}(v)\otimes\mathbf{J}_l$ and $\mathbf{A}_{\mathrm{st}}(v)$. Accordingly, the developed algorithm can be directly applied to the above-mentioned cases without modification.

IV. Simulation Results

In this part, the superiority of the proposed RACAF shaping scheme is demonstrated through computer simulations and comparing with existing schemes. We first introduce the simulation scenario and related parameter settings. Then, we validate the convergence of the proposed algorithm and

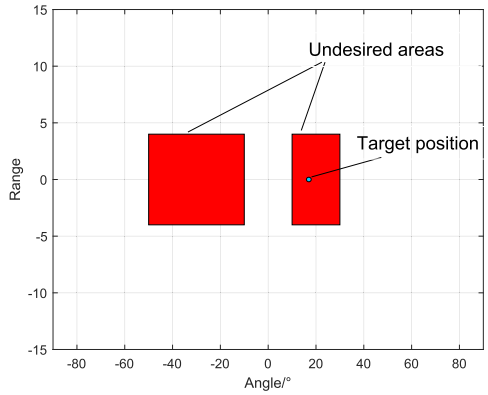

Fig. 3. Illustration of the simulation scenario.

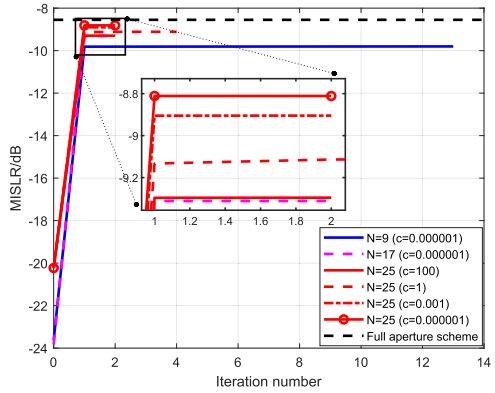

Fig. 4. MISLR versus iteration number.

analyze the RACAF optimized by the proposed scheme. Last, we compare the proposed scheme with other schemes to show improved MISLR and RACAF.

The considered range-angle interference scenario is shown in Fig. 3, where the undesired regions are marked and filled with red color. The target is located at direction 17°. Close to the target, there are strong scatterers within two regions determined by the angular region $[-50°, -10°] \cup [10°, 30°]$ and range region $[-4, 4]$. The angular regions are uniformly divided into 200 discrete points and the weighting coefficients for the undesired areas are given by

$$\eta(l, \theta_k) = \begin{cases} 1, & l \in [-4, 4],\ \theta_k \in [-50°, -10°] \cup [10°, 30°] \\ 0, & \text{else.} \end{cases} \tag{28}$$

Without loss of generality, the number of antennas at the transmit end is equal to that at the receive end, which is denoted by N. The waveform length of each transmit antenna is set as $L = 16$ and the interval between two adjacent grid points is set as half-wavelength.

A. Convergence Curves of the Proposed Method

In this example, the convergence and the monotonically increasing property of the proposed algorithm are verified. By setting $M = 33$, we show the iteration curves under $N = 9, 17$ with $c = 0.000001$, and $N = 25$ for $c = 100$, $c = 1$, $c = 0.001$, and $c = 0.000001$. The MISLR under full aperture is also added, where all the grid points are placed with antennas. As depicted in Fig. 4, the proposed algorithm monotonically converges in a few iterations at different sets

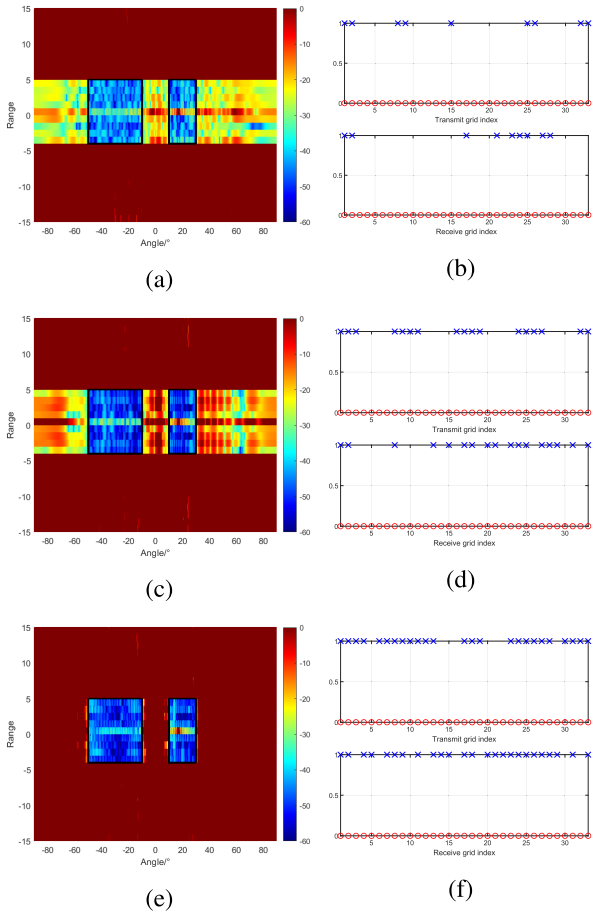

Fig. 5. Optimized array placement and RACAF. (a) and (b) $N = 9$. (c) and (d) $N = 17$. (e) and (f) $N = 25$.

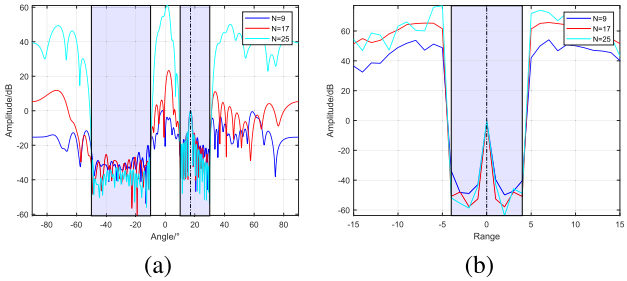

Fig. 6. Range-angle cut at target position. (a) Angular cut. (b) Range cut.

without surprise. Moreover, it is clear that a larger number of available antennas leads to a higher attainable MISLR, and less performance loss compared to the full aperture case. From Fig. 4, we also observe the impact of c on the achieved MISLR. In terms of MISLR maximization, a smaller c is preferred.

As can be seen from Fig. 5, we are displaying the optimized distribution of array antenna positions [(b), (d), (f)) and RACAFs ((a), (c), (e)] for $N = 9, 17$, and 25 with $c = 0.000001$, clear nulls are formed in the concerned areas where undesired scatters are distributed, which become deeper with more available antennas. This behavior indicates the effectiveness of the proposed scheme on suppressing signal-dependent clutter. Furthermore, a peak is formed within the region corresponding to the target position. Looking over the results of array placement after optimization unveils that

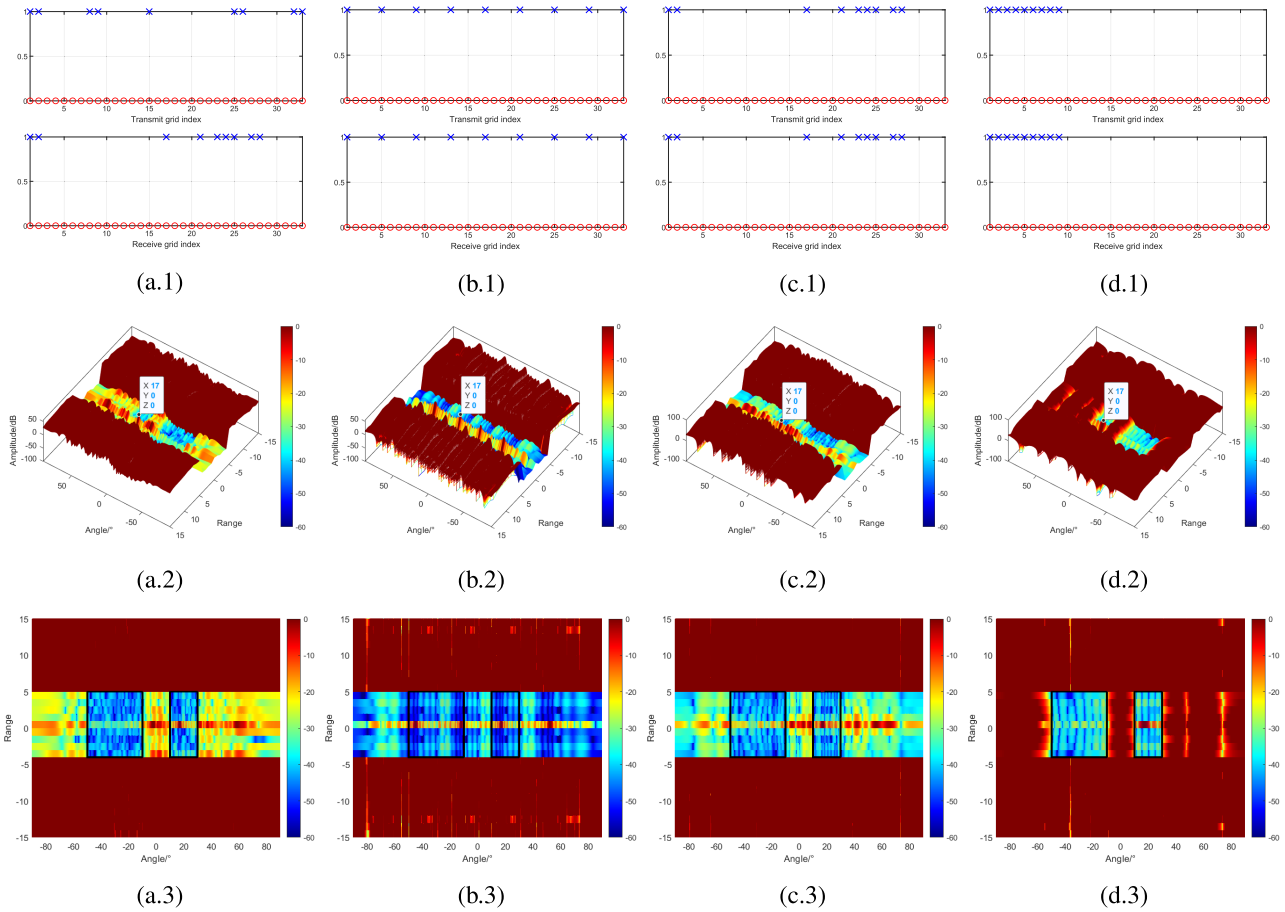

Fig. 7. RACAF and array placement comparison among different schemes. From left to right. (a) Proposed scheme. (b) Sparsely spaced scheme. (c) Randomly spaced scheme. (d) Compactly spaced scheme.

the apertures are generally larger while the inner antennas are appropriately placed, which leads to superior angular resolution. It is also noticed that the optimized configurations share a common feature about the minimal interval between two adjacent antennas, which is half-wavelength, especially for the case $N = 9$. This can be explained as if the minimum interval is larger than half-wavelength, spatial ambiguity issue would arise under the resultant array structure.

Delving deeper into the property of the range-angle response optimized by our scheme, we give the angle-cut and range-cut at target location, respectively. As given in Fig. 6(a), the results show that the sidelobes within the concerned sector $[-50°, -10°] \cup [10°, 30°]$ are effectively suppressed, while ensuring the response on target direction. It is also noticed that the spatial mainlobe of the three different cases are similar since the aperture of them are close while more number of antennas leads to deeper sidelobes. The range-cut in Fig. 6(b) indicates the sidelobes along range dimension are suppressed 50 dB lower than target position in all three cases.

B. Evaluations of Shaped Ambiguity Function

In this part, the proposed scheme is now compared against other three schemes. Specifically, with grid points fixed at $M = 33$ and given $N = 9$ antennas, we optimize the waveform and receive filter under: 1) compactly spaced scheme employed in [47]; 2) randomly spaced scheme where the antenna positions are randomly distributed among the M grids; and 3) sparsely spaced scheme where the antennas are uniformly distributed with twice wavelength interval. The corresponding array configurations have been depicted in the first column of Fig. 7. Since the main purpose of this comparison is to highlight the superiority of joint design of MIMO waveform, filter, and antenna positions, the waveform-filter pairs of the above methods are optimized by solving problem $\mathcal{P}$ with $(\mathbf{p}_t, \mathbf{p}_r)$ substituted by the comparison array structure for fairness accordingly. For easier comparison among the methods, we normalize each RACAF with its target response since we are concerning the relative suppression performance within interested areas.

The results in the second and third column of Fig. 7 provide, respectively, general and vertical view of RACAF. Generally, all the four schemes have managed to form a peak at target location while suppressing the surrounding areas. The proposed scheme and the uniform sparse array provide much sharper mainlobe thanks to the longer aperture. Note that although the randomly spaced scheme exhibits a similar mainlobe behavior as our scheme, its grating lobe caused by angular ambiguity significantly affects its target indication performance. Furthermore, while a randomly spaced array can be effective in eliminating the grating lobes, it sidelobes within $[-50°, -10°]$ are still high compared with our optimized scheme, which highlights the significance of array placement optimization. In contrast, a wide mainlobe is observed in the RACAF of the compact array due to the limited aperture.

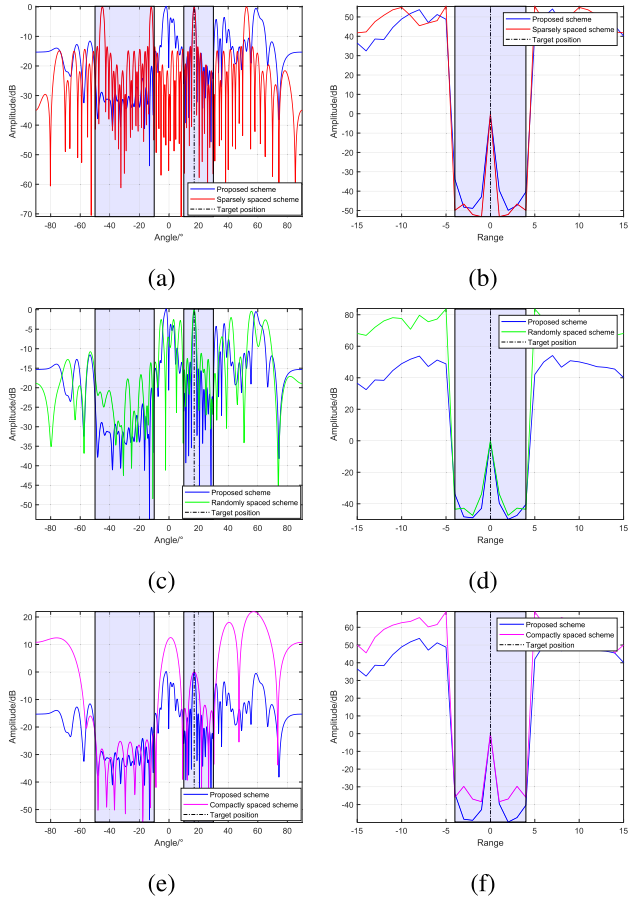

Fig. 8. Range-angle cut comparison of the RACAF at target position $(0, 17°)$.

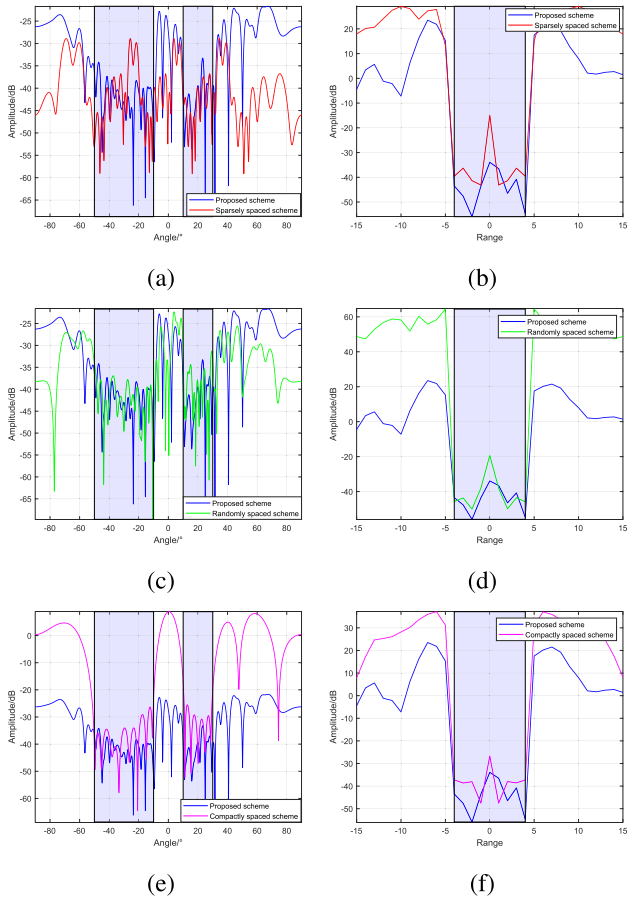

Fig. 9. Range-Angle cut comparison of the RACAF at $(3, -40°)$.

To further highlight the advantages of the proposed scheme in providing a superior target indication ability, we subsequently compare the angular-cuts and range cuts of the RACAF by different schemes at the $(0, 17°)$ (target location) and $(3, -40°)$. We first analyze the cuts at target position. As shown in Fig. 8(a) and (b), it is noticed that even though the response along the range domain is satisfactory, several grating lobes are formed along the spatial domain by the sparsely spaced scheme due to the sparse configuration, which makes its general performance deteriorates seriously. Fig. 8(c) and (d) indicates that by resorting to a random scheme, the grating lobes can be eliminated since the periodicity of the steering vector is broken. However, while its range cut behavior and mainlobe width are similar to that of the proposed scheme, its sidelobes within the concerned regions are generally much worse. From Fig. 8(e), it is observed that the compact array scheme provides satisfying notches within $[-50°, -10°]$, but its mainlobe width is large and its sidelobes within $[10°, 30°]$ are high, which leads to generally poor clutter suppression performance. In contrast, the proposed scheme enjoys a much sharper mainlobe, thanks to the optimized array structure. Moreover, the response of the compact scheme along the range domain is also limited due to the shortage of extra MIMO channels, which is almost 10 dB lower by the proposed method.

Next, we compare the sidelobe suppression performance by checking the cuts at $(3, -40°)$. As shown in Fig. 9(a), it is clearly observed that sparsely spaced scheme forms severe sidelobes with within $[-50°, -10°]$ and its range response makes it to suffer from a generally inferior performance. Compared with the randomly spaced scheme, the proposed scheme enjoys significantly improved performance along both range and angle cuts. Last, an examination of the cuts by the compact scheme reveals again the coupled relationship between the range and angular responses.

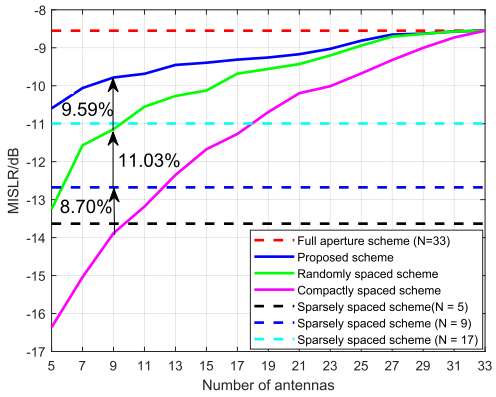

Fig. 10. Achieved MISLR versus number of antennas with $M = 33$.

C. Improvement of MISLR Over Antenna Number

In this example, we examine the impact of the antenna number on the achieved MISLR. In particular, we gradually increase the number of antennas from 5 to 33 with fixed grid

points $M = 33$ and compute the achieved MISLR. Besides the aforementioned schemes, we also consider the full aperture scheme as a benchmark for comparison, where all the grid points are placed with antennas. Since the sparsely spaced scheme is a uniform array structure, we draw the MISLR under three cases for comparison, i.e., $N = 5, 9, 17$. The array placement of the randomly spaced scheme is chosen as the initial point of the proposed scheme. As shown in Fig. 10, all listed schemes generally exhibit better performance with more available antennas. Specifically, the proposed scheme outperforms the competing schemes at all circumstances and the performance loss compared with the full aperture scheme is kept below 1.5 dB when the number of antennas is larger than 7. In comparison, the proposed scheme realizes clear improvement in MISLR over the randomly spaced scheme at all cases, which highlights again the benefits brought by array placement optimization. It is observed that through sparsely spacing the antennas to fill $M = 33$ grid points, significant performance improvement can be achieved utilizing the same number of antennas compared with the compact scheme at a low antenna number. Nevertheless, when the compact array with larger aperture is deployed, this improvement gets smaller.

V. Conclusion

The MIMO RACAF shaping problem is considered in this article, where the transmit waveform, receive filter, and antenna positions are all treated as adjustable variables for performance enhancement. It is shown that besides the waveform and filter, the range-angle behavior of MIMO radar is also closely related to array placement. Different from common AF shaping problem in the range-Doppler domain, the indefiniteness of the behavior at target location calls for a more suitable design criteria and MISLR is thereby defined to measure the sidelobe suppression performance with guaranteed target response. The joint design of MIMO transmit waveform, receive filter as well as antenna positions is formulated as a nonconvex problem and an effective algorithm is developed. In the performance assessment part, the superiority of the proposed scheme is demonstrated extensively compared to other array schemes in terms of MIMO radar RACAF shaping.

As for the future research tracks, validating the effectiveness of developed scheme on real hardware system could be of interest.

Appendix A
Proof of Proposition 1

Proof: Note that

$$\boldsymbol{\Psi}_{\text{tar}}(\mathbf{p}_\text{t}, \mathbf{p}_\text{r})\mathbf{s} = \boldsymbol{\Gamma}_{\text{tar}}(\mathbf{s}, \mathbf{p}_\text{t})\mathbf{p}_\text{r} = \boldsymbol{\Upsilon}_{\text{tar}}(\mathbf{s}, \mathbf{p}_\text{r})\mathbf{p}_\text{t} \tag{29}$$

where $\boldsymbol{\Gamma}_{\text{tar}}(\mathbf{s}, \mathbf{p}_\text{t}) = \mathbf{A}(\theta_{\text{tar}}) \otimes (\mathbf{J}_l\mathbf{S}\mathbf{A}(\theta_{\text{tar}})\mathbf{p}_\text{t})$ and $\boldsymbol{\Upsilon}_{\text{tar}}(\mathbf{s}, \mathbf{p}_\text{r}) = (\mathbf{A}(\theta_{\text{tar}})\mathbf{p}_\text{r}) \otimes (\mathbf{J}_l\mathbf{S}\mathbf{A}(\theta_{\text{tar}}))$. Similarly, we can define $\boldsymbol{\Gamma}_{l,k} = \mathbf{A}(\theta_k) \otimes (\mathbf{J}_l\mathbf{S}\mathbf{A}(\theta_k)\mathbf{p}_\text{t})$ and $\boldsymbol{\Upsilon}_{l,k} = (\mathbf{A}(\theta_k)\mathbf{p}_\text{r}) \otimes (\mathbf{J}_l\mathbf{S}\mathbf{A}(\theta_k))$ for (l, k)th range-angle patch. We first point out that through some basic algebra transformations the following equivalence chain can be easily verified:

$$\begin{aligned}\boldsymbol{\Phi}_{\text{sl}}(\mathbf{s}, \mathbf{p}_\text{t}, \mathbf{p}_\text{r}) &= \sum_{l=-L+1}^{L-1}\sum_{k=1}^{K}\eta(l, \theta_k)\boldsymbol{\Upsilon}_{l,k}(\mathbf{s}, \mathbf{p}_\text{r})\mathbf{p}_\text{t}\mathbf{p}_\text{t}^T\boldsymbol{\Upsilon}_{l,k}^H(\mathbf{s}, \mathbf{p}_\text{r}) \\ &= \sum_{l=-L+1}^{L-1}\sum_{k=1}^{K}\eta(l, \theta_k)\boldsymbol{\Gamma}_{l,k}(\mathbf{s}, \mathbf{p}_\text{t})\mathbf{p}_\text{r}\mathbf{p}_\text{r}^T\boldsymbol{\Gamma}_{l,k}^H(\mathbf{s}, \mathbf{p}_\text{t}).\end{aligned} \tag{30}$$

Moreover, leveraging on the convexity of function $g(\mathbf{a}, \mathbf{X}) = \mathbf{a}^H\mathbf{X}^{-1}\mathbf{a}$ with respect to $(\mathbf{a}, \mathbf{X})$ [64], it is easy to derive the following inequality based on the first-order approximation at any point $(\bar{\mathbf{a}}, \bar{\mathbf{X}})$ as:

$$\mathbf{a}^H\mathbf{X}^{-1}\mathbf{a} \geq -\bar{\mathbf{a}}^H\bar{\mathbf{X}}^{-1}\mathbf{X}\bar{\mathbf{X}}^{-1}\bar{\mathbf{a}} + 2\Re\left\{\bar{\mathbf{a}}^H\bar{\mathbf{X}}^{-1}\mathbf{a}\right\}. \tag{31}$$

It is seen that the right side of (31) actually provides a majorizer of $g(\mathbf{a}, \mathbf{X})$ at $(\bar{\mathbf{a}}, \bar{\mathbf{X}})$. Hence, based on the MM framework, a majorizer for the transmit array optimization objective at $\mathbf{p}_\text{t}^{(i-1)}$ can be chosen as

$$\begin{aligned}f_\text{t}(\mathbf{p}_\text{t}; \mathbf{p}_\text{t}^{(i-1)}) = &-\sum_{l=-L+1}^{L-1}\sum_{k=1}^{K}\eta(l, \theta_k)\mathbf{v}_\text{t}^{(i-1)H}\boldsymbol{\Upsilon}_{l,k}\mathbf{p}_\text{t}\mathbf{p}_\text{t}^T\boldsymbol{\Upsilon}_{l,k}^H\mathbf{v}_\text{t}^{(i-1)} \\ &+ 2\Re\left\{\mathbf{v}_\text{t}^{(i-1)H}\boldsymbol{\Upsilon}_{\text{tar}}\mathbf{p}_\text{t}\right\} - \text{Constant}\end{aligned} \tag{32}$$

where $\mathbf{v}_\text{t}^{(i-1)} = (\boldsymbol{\Phi}_{\text{sl}}(\mathbf{p}_\text{t}^{(i-1)}) + c\mathbf{I})^{-1}\boldsymbol{\Upsilon}_{\text{tar}}\mathbf{p}_\text{t}^{(i-1)}$, and $\mathbf{p}_\text{t}^{(i-1)}$ is the optimized result at the $(i-1)$th inner iteration. For notation simplicity, we have dropped the variable dependence over $\mathbf{p}_\text{r}$ and $\mathbf{s}$ with a slight abuse of denotations since they remain constant during the optimization of $\mathbf{p}_\text{t}$.

Then, mutatis mutandis, the optimization to deal with at each iteration becomes

$$\tilde{\mathcal{P}}_a\begin{cases}\max\limits_{\mathbf{p}_\text{t}} 2\Re\left\{\mathbf{v}_\text{t}^{(i-1)H}\boldsymbol{\Upsilon}_{\text{tar}}\mathbf{p}_\text{t}\right\} - \mathbf{p}_\text{t}^T\boldsymbol{\Xi}_\text{t}^{(i-1)}\mathbf{p}_\text{t} \\ \text{s.t. } p_{\text{t},m} \in \{0, 1\} \quad \forall m \\ \quad \mathbf{p}_\text{t}^T\mathbf{1} = N_\text{t}\end{cases} \tag{33}$$

where $\boldsymbol{\Xi}_\text{t}^{(i-1)} = \sum_{l=-L+1}^{L-1}\sum_{k=1}^{K}\eta(l, \theta_k)\boldsymbol{\Upsilon}_{l,k}^H\mathbf{v}_\text{t}^{(i-1)}\mathbf{v}_\text{t}^{(i-1)H}\boldsymbol{\Upsilon}_{l,k}$. Although the objective of $\tilde{\mathcal{P}}_a$ is now convex, the highly nonconvex constraints make $\tilde{\mathcal{P}}_a$ still hard to solve.

On the other hand, note that for any element within (12), one has

$$\begin{cases}\mathbf{p}_\text{r}^T\mathbf{1} = \mathbf{p}_\text{r}^T\mathbf{p}_\text{r} \\ \mathbf{p}_\text{t}^T\mathbf{1} = \mathbf{p}_\text{t}^T\mathbf{p}_\text{t}\end{cases} \tag{34}$$

which indicates

$$\begin{cases}\mathbf{p}_\text{r}^T(\mathbf{1} - \mathbf{p}_\text{r}) = \sum\limits_{m=1}^{M} p_{\text{r},m}(1 - p_{\text{r},m}) = 0 \\ \mathbf{p}_\text{t}^T(\mathbf{1} - \mathbf{p}_\text{t}) = \sum\limits_{m=1}^{M} p_{\text{t},m}(1 - p_{\text{t},m}) = 0.\end{cases} \tag{35}$$

However, since $p_{\text{r},m}, p_{\text{t},m} \in [0, 1], \forall m$, we have

$$\begin{cases}\sum\limits_{m=1}^{M} p_{\text{r},m}(1 - p_{\text{r},m}) \geq 0 \\ \sum\limits_{m=1}^{M} p_{\text{t},m}(1 - p_{\text{t},m}) \geq 0\end{cases} \tag{36}$$

and the equality holds only when $p_{\text{r},m}, p_{\text{t},m} \in \{0, 1\}, \forall m$. Therefore, we can claim that (12) is equal to

$$\begin{cases}p_{\text{r},m}, \quad p_{\text{t},m} \in \{0, 1\} \ \forall m \\ \mathbf{p}_\text{r}^T\mathbf{1} = N_\text{r}, \quad \mathbf{p}_\text{t}^T\mathbf{1} = N_\text{t} \\ \mathbf{p}_\text{r}^T\mathbf{p}_\text{r} = N_\text{r}, \quad \mathbf{p}_\text{t}^T\mathbf{p}_\text{t} = N_\text{t}.\end{cases} \tag{37}$$

Moreover, under the restrictions $p_{\mathrm{r},m}, p_{\mathrm{t},m} \in \{0,1\}, \forall m$, we have $\sum_{m=1}^{M} p_{\mathrm{t},m} = \sum_{m=1}^{M} p_{\mathrm{t},m}^2 = N_{\mathrm{t}}$ and $\sum_{m=1}^{M} p_{\mathrm{r},m} = \sum_{m=1}^{M} p_{\mathrm{r},m}^2 = N_{\mathrm{r}}$, which implies that any point within (12) satisfies condition $\mathbf{p}_{\mathrm{r}}^T \mathbf{p}_{\mathrm{r}} = N_{\mathrm{r}}, \mathbf{p}_{\mathrm{t}}^T \mathbf{p}_{\mathrm{t}} = N_{\mathrm{t}}$. Combining the discussions above, one can claim the equivalence between the set defined by (12) and that defined by following constraints:

$$\begin{cases} p_{\mathrm{r},m}, \quad p_{\mathrm{t},m} \in [0,1] \ \forall m \\ \mathbf{p}_{\mathrm{r}}^T \mathbf{1} = N_{\mathrm{r}}, \quad \mathbf{p}_{\mathrm{t}}^T \mathbf{1} = N_{\mathrm{t}} \\ \mathbf{p}_{\mathrm{r}}^T \mathbf{p}_{\mathrm{r}} = N_{\mathrm{r}}, \quad \mathbf{p}_{\mathrm{t}}^T \mathbf{p}_{\mathrm{t}} = N_{\mathrm{t}}. \end{cases} \tag{38}$$

Therefore, solving $\tilde{\mathcal{P}}_a$ is equivalent to address

$$\begin{cases} \max\limits_{\mathbf{p}_{\mathrm{t}}} 2\Re\left\{\mathbf{v}_{\mathrm{t}}^{(i-1)H} \boldsymbol{\Upsilon}_{\mathrm{tar}} \mathbf{p}_{\mathrm{t}}\right\} - \mathbf{p}_{\mathrm{t}}^T \boldsymbol{\Xi}_{\mathrm{t}}^{(i-1)} \mathbf{p}_{\mathrm{t}} \\ \text{s.t. } p_{\mathrm{t},m} \in [0,1] \quad \forall m \\ \quad \mathbf{p}_{\mathrm{t}}^T \mathbf{1} = N_{\mathrm{t}} \\ \quad \mathbf{p}_{\mathrm{t}}^T \mathbf{p}_{\mathrm{t}} = N_{\mathrm{t}}. \end{cases} \tag{39}$$

It is seen that the objective of (39) is now convex and the remaining challenge of solving (39) comes from the quadratic constraint $\mathbf{p}_{\mathrm{t}}^T \mathbf{p}_{\mathrm{t}} = N_{\mathrm{t}}$. Inspired by the feasible point pursuit idea [18], [45], [65], [66], we subsequently relax the quadratic constraint into a linear form based on the first-order approximation. In particular, in the ith iteration, we solve

$$\tilde{\mathcal{P}}_{a,\mathrm{t}}^{(i)} \begin{cases} \max\limits_{\mathbf{p}_{\mathrm{t}}, \mu_{\mathrm{t}}} 2\Re\left\{\mathbf{v}_{\mathrm{t}}^{(i-1)H} \boldsymbol{\Upsilon}_{\mathrm{tar}} \mathbf{p}_{\mathrm{t}}\right\} - \mathbf{p}_{\mathrm{t}}^T \boldsymbol{\Xi}_{\mathrm{t}}^{(i-1)} \mathbf{p}_{\mathrm{t}} - \rho_{\mathrm{t}}^{(i-1)} \mu_{\mathrm{t}} \\ \text{s.t. } p_{\mathrm{t},m} \in [0,1] \quad \forall m \\ \quad \mathbf{p}_{\mathrm{t}}^T \mathbf{1} = N_{\mathrm{t}} \\ \quad \mathbf{p}_{\mathrm{t}}^T \mathbf{p}_{\mathrm{t}} \le N_{\mathrm{t}} \\ \quad 2\mathbf{p}_{\mathrm{t}}^T \mathbf{p}_{\mathrm{t}}^{(i-1)} - \|\mathbf{p}_{\mathrm{t}}^{(i-1)}\|_2^2 \ge N_{\mathrm{t}} - \mu_{\mathrm{t}} \\ \quad \mu_{\mathrm{t}} \ge 0 \\ \quad 2\Re\left\{\mathbf{v}_{\mathrm{t}}^{(i-1)H} \boldsymbol{\Upsilon}_{\mathrm{tar}} \mathbf{p}_{\mathrm{t}}\right\} - \mathbf{p}_{\mathrm{t}}^T \boldsymbol{\Xi}_{\mathrm{t}}^{(i-1)} \mathbf{p}_{\mathrm{t}} \\ \quad \ge \widetilde{\mathrm{MISLR}}\left(\mathbf{p}_{\mathrm{t}}^{(i-1)}\right) \end{cases} \tag{40}$$

where μ_{t} represents the slack variable, $-\rho_{\mathrm{t}}^{(i-1)} \mu_{\mathrm{t}}$ is the penalty item with $\rho_{\mathrm{t}}^{(i-1)}$ being the penalty parameter, the last constraint is imposed to guarantee the MISLR at convergence is enhanced compared with its initial value. To speed up the convergence, we update the penalty parameter after each iteration. Specifically, we start the procedure from a relatively small $\rho_{\mathrm{t}}^{(0)}$, and gradually increase its value with iterations via $\rho_{\mathrm{t}}^{(i)} = \epsilon \rho_{\mathrm{t}}^{(i-1)}$ where $\epsilon > 1$ is a scalar.

The receive array optimization is similar to the transmit array optimization since they share a similar structure. In general, we can solve $\mathcal{P}_{a,\mathrm{r}}$ by iteratively solving

$$\tilde{\mathcal{P}}_{a,\mathrm{r}}^{(h)} \begin{cases} \max\limits_{\mathbf{p}_{\mathrm{r}}, \mu_{\mathrm{r}}} 2\Re\left\{\mathbf{v}_{\mathrm{r}}^{(h-1)H} \boldsymbol{\Gamma}_{\mathrm{tar}} \mathbf{p}_{\mathrm{r}}\right\} - \mathbf{p}_{\mathrm{r}}^T \boldsymbol{\Xi}_{\mathrm{r}}^{(h-1)} \mathbf{p}_{\mathrm{r}} - \rho_{\mathrm{r}}^{(h-1)} \mu_{\mathrm{r}} \\ \text{s.t. } p_{\mathrm{r},m} \in [0,1] \quad \forall m \\ \quad \mathbf{p}_{\mathrm{r}}^T \mathbf{1} = N_{\mathrm{r}} \\ \quad \mathbf{p}_{\mathrm{r}}^T \mathbf{p}_{\mathrm{r}} \le N_{\mathrm{r}} \\ \quad 2\mathbf{p}_{\mathrm{r}}^T \mathbf{p}_{\mathrm{r}}^{(h-1)} - \|\mathbf{p}_{\mathrm{r}}^{(h-1)}\|_2^2 \ge N_{\mathrm{r}} - \mu_{\mathrm{r}} \\ \quad \mu_{\mathrm{r}} \ge 0 \\ \quad 2\Re\left\{\mathbf{v}_{\mathrm{r}}^{(h-1)H} \boldsymbol{\Gamma}_{\mathrm{tar}} \mathbf{p}_{\mathrm{r}}\right\} - \mathbf{p}_{\mathrm{r}}^T \boldsymbol{\Xi}_{\mathrm{r}}^{(h-1)} \mathbf{p}_{\mathrm{r}} \\ \quad \ge \widetilde{\mathrm{MISLR}}\left(\mathbf{p}_{\mathrm{r}}^{(h-1)}\right) \end{cases} \tag{41}$$

to convergence, where $\mathbf{v}_{\mathrm{r}}^{(h-1)} = (\boldsymbol{\Phi}_{\mathrm{sl}}(\mathbf{p}_{\mathrm{r}}^{(h-1)}) + c\mathbf{I})^{-1} \boldsymbol{\Gamma}_{\mathrm{tar}} \mathbf{p}_{\mathrm{r}}^{(h-1)}$, μ_{r} represents the slack variable, $\rho_{\mathrm{r}}^{(h-1)}$ and $\mathbf{p}_{\mathrm{r}}^{(h-1)}$ are, respectively, the penalty parameter and the optimized result in the $(h-1)$th inner iteration. $\boldsymbol{\Xi}_{\mathrm{r}}^{(h-1)} = \sum_{l=-L+1}^{L-1} \sum_{k=1}^{K} \eta(l, \theta_k) \boldsymbol{\Gamma}_{l,k}^H \mathbf{v}_{\mathrm{r}}^{(h-1)} \mathbf{v}_{\mathrm{r}}^{(h-1)H} \boldsymbol{\Gamma}_{l,k}$. The derivation process is omitted for simplicity. At this point, we have successfully concluded the demonstration of Proposition 1. ■

REFERENCES

[1] J. Yang, X. Yu, M. Sha, W. Fan, and G. Cui, "Signal design for MIMO dual-function systems with permutation learning," *Sci. China Inf. Sci.*, vol. 66, no. 10, Nov. 2023, Art. no. 202303.

[2] T. Fan, G. Cui, X. Yu, Y. Bu, L. Kong, and X. Yang, "Joint design of Intra–Inter agile pulses and Doppler filter banks for Doppler ambiguous target," *IEEE Trans. Signal Process.*, vol. 72, pp. 867–882, 2024.

[3] Z. Xie, L. Wu, J. Zhu, M. Lops, X. Huang, and M. R. B. Shankar, "RIS-aided radar for target detection: Clutter region analysis and joint active-passive design," *IEEE Trans. Signal Process.*, vol. 72, pp. 1706–1723, 2024.

[4] Z. Xie, Z. Xu, S. Han, J. Zhu, and X. Huang, "Modulus constrained minimax radar code design against target interpulse fluctuation," *IEEE Trans. Veh. Technol.*, vol. 72, no. 10, pp. 13671–13676, Aug. 2023.

[5] S. D. Blunt and E. L. Mokole, "Overview of radar waveform diversity," *IEEE Aerosp. Electron. Syst. Mag.*, vol. 31, no. 11, pp. 2–42, Nov. 2016.

[6] G. Cui, A. De Maio, A. Farina, and J. Li, *Radar Waveform Design Based on Optimization Theory*. Rijeka, Croatia: SciTech, 2020.

[7] L. Wu, X. Cheng, H. Huang, D. Ciuonzo, B. Shankar, and B. Ottersten, "Constant-modulus waveform design with polarization-adaptive power allocation in polarimetric radar," *IEEE Trans. Signal Process.*, vol. 71, pp. 2146–2161, 2023.

[8] K. Zhou, S. Quan, D. Li, T. Liu, F. He, and Y. Su, "Waveform and filter joint design method for pulse compression sidelobe reduction," *IEEE Trans. Geosci. Remote Sens.*, vol. 60, pp. 1–15, 2022, Art. no. 5107615.

[9] J. Yang, Y. Tan, X. Yu, G. Cui, and D. Zhang, "Waveform design for watermark framework based DFRC system with application on joint SAR imaging and communication," *IEEE Trans. Geosci. Remote Sens.*, vol. 61, pp. 1–14, 2023, Art. no. 5200214.

[10] C. Zhang et al., "MIMO radar waveform design for simultaneous space–time–Doppler domain optimization: Framework and implementation," *IEEE Trans. Geosci. Remote Sens.*, vol. 60, pp. 1–15, 2022, Art. no. 5119415.

[11] M. Deng, Z. Cheng, L. Wu, B. Shankar, and Z. He, "One-bit ADCs/DACs based MIMO radar: Performance analysis and joint design," *IEEE Trans. Signal Process.*, vol. 70, pp. 2609–2624, 2022.

[12] G. S. Antonio, D. R. Fuhrmann, and F. C. Robey, "MIMO radar ambiguity functions," *IEEE J. Sel. Topics Signal Process.*, vol. 1, no. 1, pp. 167–177, Jun. 2007.

[13] A. Aubry, A. DeMaio, A. Farina, and M. Wicks, "Knowledge-aided (potentially cognitive) transmit signal and receive filter design in signal-dependent clutter," *IEEE Trans. Aerosp. Electron. Syst.*, vol. 49, no. 1, pp. 93–117, Jan. 2013.

[14] Z. Chen, J. Liang, T. Wang, B. Tang, and H. C. So, "Generalized MBI algorithm for designing sequence set and mismatched filter bank with ambiguity function constraints," *IEEE Trans. Signal Process.*, vol. 70, pp. 2918–2933, 2022.

[15] Z. Chen, J. Liang, K. Song, Y. Yang, and X. Deng, "On designing good Doppler tolerance waveform with low PSL of ambiguity function," *Signal Process.*, vol. 210, Sep. 2023, Art. no. 109075.

[16] G. Cui, Y. Fu, X. Yu, and J. Li, "Local ambiguity function shaping via unimodular sequence design," *IEEE Signal Process. Lett.*, vol. 24, no. 7, pp. 977–981, Jul. 2017.

[17] Y. Jing, J. Liang, B. Tang, and J. Li, "Designing unimodular sequence with low peak of sidelobe level of local ambiguity function," *IEEE Trans. Aerosp. Electron. Syst.*, vol. 55, no. 3, pp. 1393–1406, Jun. 2019.

[18] X. Yu, K. Alhujaili, G. Cui, and V. Monga, "MIMO radar waveform design in the presence of multiple targets and practical constraints," *IEEE Trans. Signal Process.*, vol. 68, pp. 1974–1989, 2020.

[19] Z. Cheng, Z. He, B. Liao, and M. Fang, "MIMO radar waveform design with PAPR and similarity constraints," *IEEE Trans. Signal Process.*, vol. 66, no. 4, pp. 968–981, Feb. 2018.

[20] J. Liu, H. Li, and B. Himed, "Joint optimization of transmit and receive beamforming in active arrays," *IEEE Signal Process. Lett.*, vol. 21, no. 1, pp. 39–42, Jan. 2014.

[21] Z. Chen, H. Li, G. Cui, and M. Rangaswamy, "Adaptive transmit and receive beamforming for interference mitigation," *IEEE Signal Process. Lett.*, vol. 21, no. 2, pp. 235–239, Feb. 2014.

[22] R. Liu et al., "Transmit-receive beamforming for distributed phased-MIMO radar system," *IEEE Trans. Veh. Technol.*, vol. 71, no. 2, pp. 1439–1453, Feb. 2022.

[23] J. Song, P. Babu, and D. P. Palomar, "Sequence design to minimize the weighted integrated and peak sidelobe levels," *IEEE Trans. Signal Process.*, vol. 64, no. 8, pp. 2051–2064, Apr. 2016.

[24] J. Song, P. Babu, and D. P. Palomar, "Optimization methods for designing sequences with low autocorrelation sidelobes," *IEEE Trans. Signal Process.*, vol. 63, no. 15, pp. 3998–4009, Aug. 2015.

[25] Q. Liu, W. Ren, K. Hou, T. Long, and A. E. Fathy, "Design of polyphase sequences with low integrated sidelobe level for radars with spectral distortion via majorization-minimization framework," *IEEE Trans. Aerosp. Electron. Syst.*, vol. 57, no. 6, pp. 4110–4126, Dec. 2021.

[26] M. A. Kerahroodi, A. Aubry, A. De Maio, M. M. Naghsh, and M. Modarres-Hashemi, "A coordinate-descent framework to design low PSL/ISL sequences," *IEEE Trans. Signal Process.*, vol. 65, no. 22, pp. 5942–5956, Nov. 2017.

[27] M. Alaee-Kerahroodi, L. Wu, E. Raei, and M. R. B. Shankar, "Joint waveform and receive filter design for pulse compression in weather radar systems," *IEEE Trans. Radar Syst.*, vol. 1, pp. 212–229, Jun. 2023.

[28] X. Yu, T. Fan, H. Qiu, R. Wang, G. Cui, and L. Kong, "Constrained transceiver design with expanded mainlobe for range sidelobe reduction," *IEEE Trans. Aerosp. Electron. Syst.*, vol. 58, no. 5, pp. 4803–4813, Oct. 2022.

[29] Y. Gao, H. Fan, L. Ren, Z. Liu, Q. Liu, and E. Mao, "Joint design of waveform and mismatched filter for interrupted sampling repeater jamming suppression," *IEEE Trans. Aerosp. Electron. Syst.*, vol. 59, no. 6, pp. 8037–8050, Dec. 2023.

[30] H. V. Trees et al., *Optimum Array Processing*. New York, NY, USA: Wiley, 2002.

[31] H. Huang, H. C. So, and A. M. Zoubir, "Sparse array beamformer design via ADMM," *IEEE Trans. Signal Process.*, vol. 71, pp. 3357–3372, 2023.

[32] T. Wei, L. Wu, and B. M. R. Shankar, "Sparse array beampattern synthesis via majorization-based ADMM," in *Proc. IEEE 94th Veh. Technol. Conf. (VTC-Fall)*, Sep. 2021, pp. 1–5.

[33] S. Sanayei and A. Nosratinia, "Antenna selection in MIMO systems," *IEEE Commun. Mag.*, vol. 42, no. 10, pp. 68–73, Oct. 2004.

[34] H. Huang, L. Wu, B. Shankar, and A. M. Zoubir, "Sparse array design for dual-function radar-communications system," *IEEE Commun. Lett.*, vol. 27, no. 5, pp. 1412–1416, May 2023.

[35] Z. Yang, Q. Shen, W. Liu, Y. C. Eldar, and W. Cui, "High-order cumulants based sparse array design via fractal geometries—Part I: Structures and DOFs," *IEEE Trans. Signal Process.*, vol. 71, pp. 327–342, 2023.

[36] M. Huan, J. Liang, Y. Wu, Y. Li, and W. Liu, "SASA: Super-resolution and ambiguity-free sparse array geometry optimization with aperture size constraints for MIMO radar," *IEEE Trans. Antennas Propag.*, vol. 71, no. 6, pp. 4941–4954, Mar. 2023.

[37] P. Gupta and M. Agrawal, "Design and analysis of the sparse array for DoA estimation of noncircular signals," *IEEE Trans. Signal Process.*, vol. 67, no. 2, pp. 460–473, Jan. 2019.

[38] J. Zhang and W. Liu, "Antenna selection for multi-beam multiplexing design based on the hybrid beamforming architecture," in *Proc. IEEE Stat. Signal Process. Workshop (SSP)*, Jul. 2021, pp. 261–265.

[39] S. A. Hamza and M. G. Amin, "Hybrid sparse array beamforming design for general rank signal models," *IEEE Trans. Signal Process.*, vol. 67, no. 24, pp. 6215–6226, Dec. 2019.

[40] S. A. Hamza and M. G. Amin, "Sparse array beamforming design for wideband signal models," *IEEE Trans. Aerosp. Electron. Syst.*, vol. 57, no. 2, pp. 1211–1226, Apr. 2021.

[41] M. B. Hawes and W. Liu, "Location optimization of robust sparse antenna arrays with physical size constraint," *IEEE Antennas Wireless Propag. Lett.*, vol. 11, pp. 1303–1306, 2012.

[42] S. Shrestha, X. Fu, and M. Hong, "Optimal solutions for joint beamforming and antenna selection: From branch and bound to graph neural imitation learning," *IEEE Trans. Signal Process.*, vol. 71, pp. 831–846, 2023.

[43] A. M. Elbir, K. V. Mishra, and Y. C. Eldar, "Cognitive radar antenna selection via deep learning," *IET Radar, Sonar Navigat.*, vol. 13, no. 6, pp. 871–880, Jun. 2019.

[44] X. Wang, M. Amin, and X. Cao, "Analysis and design of optimum sparse array configurations for adaptive beamforming," *IEEE Trans. Signal Process.*, vol. 66, no. 2, pp. 340–351, Jan. 2018.

[45] X. Yu, H. Qiu, J. Yang, W. Wei, G. Cui, and L. Kong, "Multi-spectrally constrained MIMO radar beampattern design via sequential convex approximation," *IEEE Trans. Aerosp. Electron. Syst.*, vol. 58, no. 4, pp. 2935–2949, Aug. 2022.

[46] A. Aubry, A. De Maio, and Y. Huang, "MIMO radar beampattern design via PSL/ISL optimization," *IEEE Trans. Signal Process.*, vol. 64, no. 15, pp. 3955–3967, Aug. 2016.

[47] L. Wu, P. Babu, and D. P. Palomar, "Transmit waveform/receive filter design for MIMO radar with multiple waveform constraints," *IEEE Trans. Signal Process.*, vol. 66, no. 6, pp. 1526–1540, Mar. 2018.

[48] X. Yu, G. Cui, J. Yang, and L. Kong, "MIMO radar transmit–receive design for moving target detection in signal-dependent clutter," *IEEE Trans. Veh. Technol.*, vol. 69, no. 1, pp. 522–536, Jan. 2020.

[49] B. Tang and J. Tang, "Joint design of transmit waveforms and receive filters for MIMO radar space-time adaptive processing," *IEEE Trans. Signal Process.*, vol. 64, no. 18, pp. 4707–4722, Sep. 2016.

[50] B. Tang and J. Li, "Spectrally constrained MIMO radar waveform design based on mutual information," *IEEE Trans. Signal Process.*, vol. 67, no. 3, pp. 821–834, Feb. 2019.

[51] G. Sun, Z. He, J. Tong, X. Yu, and S. Shi, "Mutual information-based waveform design for MIMO radar space-time adaptive processing," *IEEE Trans. Geosci. Remote Sens.*, vol. 59, no. 4, pp. 2909–2921, Apr. 2021.

[52] Z.-J. Wu, C.-X. Wang, Y.-C. Li, and Z.-Q. Zhou, "Extended target estimation and recognition based on multimodel approach and waveform diversity for cognitive radar," *IEEE Trans. Geosci. Remote Sens.*, vol. 60, pp. 1–14, 2022, Art. no. 5101014.

[53] Z. Cheng, Y. Lu, Z. He, Yufengli, J. Li, and X. Luo, "Joint optimization of covariance matrix and antenna position for MIMO radar transmit beampattern matching design," in *Proc. IEEE Radar Conf. (RadarConf18)*, Apr. 2018, pp. 1073–1077.

[54] M. Deng, Z. Cheng, and Z. He, "Co-Design of waveform correlation matrix and antenna positions for MIMO radar transmit beampattern formation," *IEEE Sens. J.*, vol. 20, no. 13, pp. 7326–7336, Jul. 2020.

[55] A. Bose, S. Khobahi, and M. Soltanalian, "Joint optimization of waveform covariance matrix and antenna selection for MIMO radar," in *Proc. 53rd Asilomar Conf. Signals, Syst., Comput.*, Nov. 2019, pp. 1534–1538.

[56] A. Bose, S. Khobahi, and M. Soltanalian, "Efficient waveform covariance matrix design and antenna selection for MIMO radar," *Signal Process.*, vol. 183, Jun. 2021, Art. no. 107985.

[57] M. I. Skolnik, *Radar Handbook*. New York, NY, USA: McGraw-Hill, 1970.

[58] M. A. Richards, *Fundamentals of Radar Signal Processing*. New York, NY, USA: McGraw-Hill, 2014.

[59] J. Yang, G. Cui, X. Yu, and L. Kong, "Dual-use signal design for radar and communication via ambiguity function sidelobe control," *IEEE Trans. Veh. Technol.*, vol. 69, no. 9, pp. 9781–9794, Sep. 2020.

[60] P. Stoica, H. He, and J. Li, "New algorithms for designing unimodular sequences with good correlation properties," *IEEE Trans. Signal Process.*, vol. 57, no. 4, pp. 1415–1425, Apr. 2009.

[61] L. Wu, P. Babu, and D. P. Palomar, "Cognitive radar-based sequence design via SINR maximization," *IEEE Trans. Signal Process.*, vol. 65, no. 3, pp. 779–793, Feb. 2017.

[62] R. A. Horn and C. R. Johnson, *Matrix Analysis*. Cambridge, U.K.: Cambridge Univ. Press, 2012.

[63] M. Grant and S. Boyd. (2014). *CVX: MATLAB Software for Disciplined Convex Programming, Version 2.1*. [Online]. Available: https://cvxr.com/cvx/

[64] S. Boyd, S. P. Boyd, and L. Vandenberghe, *Convex Optimization*. Cambridge, U.K.: Cambridge Univ. Press, 2004.

[65] O. Mehanna, K. Huang, B. Gopalakrishnan, A. Konar, and N. D. Sidiropoulos, "Feasible point pursuit and successive approximation of non-convex QCQPs," *IEEE Signal Process. Lett.*, vol. 22, no. 7, pp. 804–808, Jul. 2015.

[66] Z. Xie, Z. Xu, C. Fan, S. Han, and X. Huang, "Robust radar waveform optimization under target interpulse fluctuation and practical constraints via sequential Lagrange dual approximation," *IEEE Trans. Aerosp. Electron. Syst.*, vol. 59, no. 6, pp. 9711–9721, Aug. 2023.

Zhuang Xie received the B.S. degree in electronic information engineering from Harbin Institute of Technology, Harbin, China, in 2018, and the M.S. degree in information and communication engineering from the National University of Defense Technology, Changsha, China, in 2020, where he is currently pursuing the Ph.D. degree.

His research interests include radar signal processing and optimization theory, with emphasis on radar waveform design.

Linlong Wu (Senior Member, IEEE) received the B.E. degree in electronic information from Xi'an Jiaotong University (XJTU), Xi'an, China, in 2014, and the Ph.D. degree in electronic and computer engineering from Hong Kong University of Science and Technology (HKUST), Hong Kong, in 2018.

He was with the Wireless Network Group of Alibaba Cloud, Hangzhou, China, from November 2018 to October 2020 as a Research Engineer working on designing and building commercial RFID-based localization systems. Since November, 2020, he has been with the Interdisciplinary Center for Security, Reliability and Trust (SnT), University of Luxembourg, Esch-sur-Alzette, Luxembourg, where he is currently a Research Scientist with the Signal Processing Applications in Radar and Communications (SPARC) Group. His research interests include signal processing, optimization, and machine learning with applications in waveform design, integrated sensing, and communication and IoT networks.

Xiaotao Huang (Senior Member, IEEE) received the B.S. and Ph.D. degrees in information and communications engineering from National University of Defense Technology, Changsha, China, in 1990 and 1999, respectively.

He is currently a Professor with National University of Defense Technology. His research interests include radar theory, signal processing, and radio frequency signal suppression.

Chongyi Fan received the B.Eng. degree in electrical and electronic engineering and the Ph.D. degree in information and communication engineering from the National University of Defense Technology (NUDT), Changsha, China, in 2006 and 2012, respectively.

She is currently an Associate Professor with the College of Electronic Science and Engineering, NUDT. She teaches the courses of Array Signal Processing, Introduction of New Concept Radar and Signal and System. Her research interests include convex optimization, MIMO radar, and array signal processing.

Jiahua Zhu (Senior Member, IEEE) received the B.S. degree in electronic engineering and the Ph.D. degree in information and communication engineering from the National University of Defense Technology, Changsha, China, in 2012 and 2018, respectively.

He is currently an Associate Professor and the Master Supervisor with the College of Meteorology and Oceanography, National University of Defense Technology. From November 2015 to November 2017, he was a Visiting Ph.D. Student with the School of Engineering, RMIT University, Melbourne, VIC, Australia, and the Department of Electrical and Electronic Engineering, University of Melbourne, Melbourne. His research interests include waveform design and target detection for radar and sonar.

Dr. Zhu received the Best Paper Award in the Ninth Research Symposium for Chinese Ph.D. Students and Scholars in Australia, in 2016, the Excellent Paper Award in 2021 IEEE/OES China Ocean Acoustics Conference, and the outstanding Ph.D. degree thesis of the Chinese People's Liberation Army (PLA), in 2020. He is a Program Co-Chair and the Regional Chair of IEEE International Conference on Signal and Image Processing (ICSIP), an Editorial Board Member of IEEE SIGNAL PROCESSING LETTERS and *IET Signal Processing*, a Topical Advisory Panel Member and the Lead Guest Editor of *Remote Sensing*, and the Guest Editor of IEEE JOURNAL OF SELECTED TOPICS IN APPLIED EARTH OBSERVATIONS AND REMOTE SENSING.

Wei Liu (Senior Member, IEEE) received the B.Sc. degree in space physics and the L.L.B. degree intellectual property law degree from Peking University, Beijing, China, in 1996 and 1997, respectively, the M.Phil. degree from the Department of Electrical and Electronic Engineering, University of Hong Kong, Hong Kong, in 2000, and the Ph.D. degree from the School of Electronics and Computer Science, University of Southampton, Southampton, U.K., in 2003.

Then, he worked as a postdoctoral position first at the University of Southampton and later at Imperial College London, London, U.K. From 2005 to 2023, he was with the Department of Electronic and Electrical Engineering, University of Sheffield, Sheffield, U.K., first as a Lecturer and then a Senior Lecturer. Since September 2024, he has been a Reader at the School of Electronic Engineering and Computer Science, Queen Mary University of London, London. He has published more than 400 journal and conference papers, six book chapters, and two research monographs titled "Wideband Beamforming: Concepts and Techniques" (Wiley, March 2010) and "Low-Cost Smart Antennas" (Wiley, March 2019), respectively. His research interests include a wide range of topics in signal processing, with a focus on sensor array signal processing and its various applications, such as robotics and autonomous systems, human computer interface, radar, sonar, and wireless communications.

Dr. Liu is a member of the Applied Signal Processing Systems Technical Committee (2023–2025) of the IEEE Signal Processing Society (SPS), the Digital Signal Processing Technical Committee of the IEEE Circuits and Systems Society (Chair for 2022–2024), and the IEEE SPS Education Board (2024–2026, Chair of its Educational Conference Program Committee), and a former member of the Sensor Array and Multichannel Signal Processing Technical Committee of the IEEE SPS (Chair for 2021–2022), the IEEE SPS Technical Directions Board (2021–2022), and the IEEE SPS Conference Board and its Executive Subcommittee (2022–2023). He also acted as an Associate Editor of IEEE TRANSACTION ON SIGNAL PROCESSING, IEEE ACCESS, and *Journal of the Franklin Institute*. He is currently an Associate Editor of IEEE ANTENNAS AND WIRELESS PROPAGATION LETTERS, and an Executive Associate Editor-in-Chief of the *Frontiers of Information Technology and Electronic Engineering*. He is an IEEE Distinguished Lecturer of the Aerospace and Electronic Systems Society (2023–2024).